

# LOCALIZATION OF TUMOR THROUGH A NON-CONVENTIONAL NUMERICAL SHAPE OPTIMIZATION TECHNIQUE

JULIUS FERGY TIONGSON RABAGO

**ABSTRACT.** This paper introduces a method for estimating the shape and location of an embedded tumor. The approach utilizes shape optimization techniques, applying the coupled complex boundary method. By rewriting the problem—characterized by a measured temperature profile and corresponding flux (e.g., from infrared thermography)—into a complex boundary value problem with a complex Robin boundary condition, the method simplifies the over-specified nature of the problem. The size and location of the tumor are identified by optimizing a cost function based on the imaginary part of the solution across the domain. Shape sensitivity analysis is conducted to compute the shape derivative of the functional. An iterative algorithm, which uses the Riesz representative of the gradient, is developed to numerically determine the geometry of the tumor via the finite element method. Additionally, we analyze the mesh sensitivity of the finite element solution of the associated state problem and derive a bound on its variation in terms of mesh deformation and its gradient. The result, valid in any dimension, applies to arbitrary unstructured simplicial meshes and finite element approximations. Numerical examples are provided to validate the theoretical findings and demonstrate the feasibility of the proposed method.

## 1. INTRODUCTION

Body temperature is widely recognized as a key health indicator. Generally, the surface temperature of the skin is influenced by underlying blood circulation, local metabolic activity, and heat exchange between the skin and its environment [Cha85, Bow85]. Variations in any of these factors can alter skin surface temperature and heat flux, reflecting the body’s physiological state. Tumors, due to their unique structure and angiogenesis processes, often exhibit abnormal behavior. Features such as inflammation, increased metabolic rates, interstitial hypertension, abnormal blood vessel morphology, and a lack of homeostatic regulation contribute to tumors generating and dissipating heat differently compared to normal tissue. For instance, skin temperature above a tumor, such as a malignant melanoma or breast tumor, is often significantly higher than that of surrounding tissues [KKBS22, Law56, LC63, MB95, BM<sup>+</sup>09].

This abnormal surface temperature can be used to estimate the location and size of tumors and to monitor their evolution after treatment. Medical infrared thermography, a non-invasive and contact-free imaging method, measures radiation emitted from the skin and detects subtle temperature changes. Although thermography’s early medical applications were limited by the high cost, complexity, and low sensitivity of older infrared cameras, recent advancements have renewed its potential as a valuable tool for examining superficial tissues and the vascular, neurogenic, and metabolic processes affecting them. For example, Santa Cruz et al. [BM<sup>+</sup>09] demonstrated the capability of thermography to identify regions of acute skin reaction following boron neutron capture therapy (BNCT) and to correlate these areas with dose distributions. Their findings suggest that thermography can aid in locating regions of high temperature or melanoma nodules undetectable in CT imaging.

This study aims to develop a numerical method for estimating the location and size of an embedded malignant melanoma tumor based on abnormal skin surface temperature profiles. The problem is modeled using Pennes’ bioheat equation [Pen48] under suitable boundary conditions. Pennes’ equation models heat transfer in living tissues, accounting for varying thermal properties and heat sources in healthy and tumor regions [Law56, LC63, MB95, BM<sup>+</sup>09]. We assume

piecewise constant properties, framing the problem as identifying the tumor shape  $\bar{\Omega}_0 \subset \Omega$ , where  $\Omega$  is the tissue region, using boundary temperature data  $\partial\Omega$ . A non-conventional shape optimization method [DZ11, HP18, SZ92, MS76] is employed. We first address the inverse geometry problem by converting the measured temperature profile and heat flux (e.g., from infrared thermography) into a Robin boundary condition. The target shape is found by minimizing a functional based on the imaginary part of the solution, using shape calculus. Numerical solution of the resulting minimization problem relies on information about the *Eulerian* derivative of the shape functional, also known as the *shape gradient*.

In shape calculus, the *Eulerian* derivative [DZ11, p. 471] of a shape functional can be expressed in either distributed [LS16] or boundary form [DZ11, HP18, SZ92]. The boundary form, derived from the Hadamard-Zolésio structure theorem [DZ11, Thm. 3.6, p. 479], is notable in numerical shape optimization due to its concise representation [MP01, SSW15]. However, finite element approximations of this form are not suitable for irregular boundaries. The distributed Eulerian derivative, being more broadly applicable [LS16], warrants greater consideration in numerical computations.

This work employs finite element methods (FEMs) for numerical computations. The motivation for this approach is discussed in subsection 4.1. FEMs are widely used in shape optimization to discretize and solve PDEs on arbitrary domains [MP01]. Accurate numerical shape gradients are crucial for optimization algorithms [DZ11], particularly in geometric inverse problems. Distributed shape gradient algorithms are preferable to surface-based ones, as they improve finite element mesh quality and enhance efficiency, as shown in [SSW15, LS16], where numerical comparisons confirm the robustness and efficiency of the distributed approach. In [HPS15], the distributed Eulerian derivative demonstrates faster convergence and higher accuracy for elliptic problems. In this work, shape gradient information will be obtained using Delfour-Zolésio's minimax formulation approach [DZ88]. This approach, in contrast to the chain rule method, avoids the need to compute material or shape derivatives of the states. It is a well-established method, frequently used in optimal shape design and control theory [Aze20]. However, its application in shape sensitivity analysis is not straightforward due to the pseudo-time dependence of the function spaces in the minimax formulation. To address this, two methods are available [DZ11, DZ88]: the function space parameterization and the function embedding technique. In this study, we will apply the former.

*Paper organization.* Following the medical context of skin cancer and its thermal characteristics, the remainder of this paper is organized as follows: Section 2 describes the mathematical model for heat transfer in the human body. Section 3 formulates the inverse problem. Section 4 introduces the coupled complex boundary method (CCBM) and the resulting shape optimization problem, where we clarify the motivation and contribution of this study. Section 5 presents the computation of the shape derivative of the corresponding cost functional in the CCBM formulation. Section 6 some tools needed to examine mesh deformations. Section 7 conducts a mesh sensitivity analysis for the finite element solution of the state problem. Section 8 briefly discusses the discretization of the objective function and highlights key considerations for using the volume expression in shape gradient calculations. Section 9 details the numerical implementation of our approach and presents simulations, including cases with and without random noise in both two and three dimensions, to evaluate the algorithm's performance. Finally, Section 10 concludes with final remarks. An appendix is provided with key results used in the study and proofs of some lemmas.

**Acknowledgements** This work is partially supported by the JSPS Postdoctoral Fellowships for Research in Japan (under Project Number 24KF0221) and by the JSPS Grant-in-Aid for Early-Career Scientists under Japan Grant Number JP23K13012 and the JST CREST Grant Number JPMJCR2014.

## 2. THE MODEL EQUATION

**2.1. The bioheat transfer problem.** Since Pennes' landmark paper in 1948 [Pen48], several bioheat transfer equations for living tissues have been proposed. The key theoretical contribution of Pennes' work is the idea that the heat transfer rate between blood and tissue is proportional to the product of the volumetric perfusion rate and the temperature difference between arterial blood and local tissue. This relationship is expressed as:

$$h_b = G_b \rho_b c_b (1 - \kappa)(T_b - u),$$

where the parameters are defined as follows:  $h_b$  represents the heat transfer rate per unit volume of tissue,  $G_b$  denotes the perfusion rate per unit volume,  $\rho_b$  is the blood density,  $c_b$  is the blood's specific heat,  $\kappa$  is a factor for incomplete thermal equilibrium between blood and tissue,  $T_b$  is the arterial blood temperature, and  $u$  represents the local tissue temperature. The parameter  $\kappa$  can range from 0 to 1. However, Pennes assumed  $\kappa = 0$  in his model [Pen48], treating the arterial temperature as constant and equal to the core body temperature.

Pennes' equation accounts for heat conduction through tissue and the generation of heat from metabolic activity. When combined with heat transfer due to blood circulation, the steady-state equation becomes:

$$-\nabla \cdot (\sigma(x) \nabla u(x)) + k(x)(u(x) - T_b) = q(x), \quad x \in \Omega \subset \mathbb{R}^d, \quad d \in \{2, 3\},$$

In this equation,  $\sigma$  represents the thermal conductivity,  $k = G_b \rho_b c_b$  is the perfusion coefficient,  $q$  denotes the metabolic heat source, and  $T_b$  is the constant blood temperature. Hereinafter, for simplicity, we denote  $Q = q + kT_b$ .

Using the fact that the thermal conductivity, perfusion, and metabolic activity in a melanoma tumor are significantly higher than in normal tissue (see, e.g., [DB71, SLR<sup>+</sup>84]), we consider all these coefficients to be *piecewise* defined. More precisely, we define the coefficients as follows:

$$\sigma(x) = \begin{cases} \sigma_1, & \text{if } x \in \Omega_1, \\ \sigma_0, & \text{if } x \in \Omega_0, \end{cases} \quad k(x) = \begin{cases} k_1, & \text{if } x \in \Omega_1, \\ k_0, & \text{if } x \in \Omega_0, \end{cases} \quad Q(x) = \begin{cases} Q_1, & \text{if } x \in \Omega_1, \\ Q_0, & \text{if } x \in \Omega_0, \end{cases} \quad (1)$$

where  $\Omega_0$  represents the tumor region and  $\Omega_1$  represents the healthy tissue (see Figure 1).

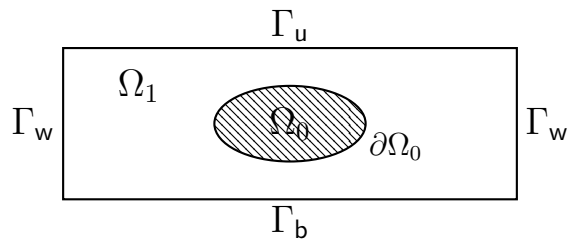


FIGURE 1. Two dimensional illustration

In this study, a single embedded tumor is assumed within the entire domain, surrounded by healthy tissue. Transmission conditions are applied on  $\partial\Omega_0$ , with different boundary conditions on sections of  $\partial\Omega$ , which consists of three main parts:  $\Gamma_u$ ,  $\Gamma_w$ , and  $\Gamma_b$ . Specifically, a constant core temperature  $T_b > 0$  is assumed at the bottom boundary  $\Gamma_b$ . An adiabatic condition is used on the lateral boundaries  $\Gamma_w$ , assuming that the temperature field is minimally influenced by central sources or distant external heating/cooling. A convective condition is applied on the upper boundary  $\Gamma_u$  to model heat exchange between the body and the environment.

Mathematically, defining  $u_1 = u|_{\Omega_1}$  and  $u_0 = u|_{\Omega_0}$ , we arrive at the following transmission problem:

$$\begin{cases} -\sigma_1 \Delta u_1 + k_1 u_1 = Q_1, & \text{in } \Omega_1, \\ -\sigma_0 \Delta u_0 + k_0 u_0 = Q_0, & \text{in } \Omega_0, \\ u_1 = u_0, & \text{on } \partial\Omega_0, \\ -\sigma_1 \frac{\partial u_1}{\partial n} = -\sigma_0 \frac{\partial u_0}{\partial n}, & \text{on } \partial\Omega_0, \\ -\sigma_1 \frac{\partial u_1}{\partial n} = \alpha(u_1 - T_a), & \text{on } \Gamma_u, \\ -\sigma_1 \frac{\partial u_1}{\partial n} = 0, & \text{on } \Gamma_w, \\ u_1 = T_b, & \text{on } \Gamma_b, \end{cases} \quad (2)$$

where  $\alpha$  is the heat transfer coefficient,  $T_a$  is the ambient temperature,  $\Omega_1$  represents the domain of healthy tissue,  $\Omega_0$  denotes the tumor domain, and  $n$  is the outward-pointing unit normal.

Evaporation on the skin surface can also be considered. In this case, a time-dependent heat equation must be used, as the humidity coefficient varies with time.

**2.2. Notations.** In this study, we mainly work on complex versions of Sobolev and Lebesgue spaces, as the proposed method requires complex-valued functions. We will not, however, distinguish between spaces of real and complex functions, as the context will clarify their use.

Let  $d \in \{2, 3\}$  denote the spatial dimension. We define  $\partial_i := \partial/\partial x_i$  and  $\nabla := (\partial_1, \dots, \partial_d)^\top$ . Also,  $\partial_n := \partial/\partial n = \sum_{i=1}^d n_i \partial_i$ , where  $n \in \mathbb{R}^d$  is the outward unit normal vector to  $\Omega$ . The inner product of  $a, b \in \mathbb{R}^d$  is  $a \cdot b := a^\top b \equiv \langle a, b \rangle$ , and we use  $\varphi_n$  for  $\varphi \cdot n$  when convenient.

For a vector-valued function  $\varphi := (\varphi_1, \dots, \varphi_d)^\top : \Omega \rightarrow \mathbb{R}^d$ ,  $(\nabla \varphi)_{ij} := (\partial_i \varphi_j)_{i,j=1,\dots,d}$  represents its gradient, while its Jacobian is  $(D\varphi)_{ij} = (\partial_j u_i)_{i,j=1,\dots,d} \equiv \nabla^\top \varphi$ . Thus,  $\partial_n \varphi := (D\varphi)n$ .

Let  $m \in \mathbb{N} \cup \{0\}$ . The spaces  $L^2(\Omega)$  and  $H^m(\Omega) = W^{m,2}(\Omega)$  denote real Lebesgue and Sobolev spaces with natural norms. The space  $H^m(\Omega)^d$  consists of vector-valued functions  $\varphi : \Omega \rightarrow \mathbb{R}^d$  with  $u_i \in H^m(\Omega)$  for  $i = 1, \dots, d$ , and its norm is  $\|\varphi\|_{H^m(\Omega)^d} := \left( \sum_{i=1}^d \|u_i\|_{H^m(\Omega)}^2 \right)^{1/2}$ .

For the complex version, we define the inner product  $((\varphi, \psi))_{m,\Omega,d} = \sum_{j=1}^d (\varphi, \bar{\psi})_{m,\Omega}$  and the norm  $\|\psi\|_{m,\Omega,d} = \sqrt{((\psi, \bar{\psi}))_{m,\Omega,d}}$ . For real-valued functions,  $\|\cdot\|_{m,\Omega,d} = \|\cdot\|_{W^{m,p}(\Omega)}$ . Here,  $\bar{\varphi}$  denotes the complex conjugate of  $\varphi$ , and ‘ $\cdot$ ’ denotes the Frobenius inner product:  $\nabla \varphi \cdot \nabla \psi = \sum_{i,j=1}^d \partial_i \varphi_j \partial_i \bar{\psi}_j$ . The spaces in discrete setting, as understood in the present study, are also understood to be complex-valued.

For later use, we also denote by  $n$  the outward unit normal to  $\partial\Omega_0$  pointing into  $\Omega_1$ . We define  $\partial_n u_0$  (respectively,  $\partial_n u_1$ ) as the normal derivative from inside  $\Omega_0$  (respectively,  $\Omega_1$ ) at  $\partial\Omega_1$ , and  $[\cdot]$  represents the jump across this interface. We occasionally write  $\int_\Omega \cdot dx$  instead of  $\int_{\Omega_1} \cdot dx + \int_{\Omega_0} \cdot dx$  when it causes no confusion.

**2.3. Weak formulation of the problem.** In this investigation, we generally assume that

- Assumption 2.1.** (A1)  $\Omega \subset \mathbb{R}^d$ ,  $d \in \{2, 3\}$ , is a bounded domain of class  $C^{k,1}$ ,  $k \in \mathbb{N}$ ;  
 (A2)  $\Omega$  contains a  $C^{k,1}$  subdomain  $\omega \Subset \Omega$  characterized by a finite jump in the coefficients of the PDE such that  $\Omega \setminus \bar{\omega}$  is connected;  
 (A3)  $\sigma_0, \sigma_1 \in W^{1,\infty}(\Omega)$  and  $\sigma_0, \sigma_1 > 0$ ;  
 (A4)  $k_0, k_1 \in W^{1,\infty}(\Omega)$  and  $k_0, k_1 > 0$ ;  
 (A5)  $Q_0, Q_1 \in H^1(\Omega)$ .

For later reference and technical purposes, especially in Section 7, we assume the existence of constants  $\underline{\sigma}, \bar{\sigma}, \underline{k}, \bar{k} > 0$  such that for almost every  $x \in \Omega$ , the following inequalities hold:

$$\underline{\sigma} \leq \sigma(x) \leq \bar{\sigma} \quad \text{and} \quad \underline{k} \leq k(x) \leq \bar{k}. \quad (3)$$

The regularity of the piecewise-defined coefficients given in (A3) and (A4) of Assumption 2.1 is more than what is necessary for some preliminary results, such as Proposition 4.5. In fact, to prove Proposition 4.5, it suffices to assume that the coefficients belong to the  $L_+^\infty$  space, which denotes the subset of  $L^\infty$  functions with positive essential infima. Generally, we may assume that  $\alpha \in L_+^\infty(\Gamma_u)$ ,  $T_a \in H^{-1/2}(\Gamma_u)$ ,  $T_b \in H^{1/2}(\Gamma_b)$ , and  $Q \in L^2(\Omega)$ —at least for the *well-posedness* of the weak form of the direct problem. For most results and for simplicity, we treat  $\alpha$ ,  $T_a$ , and  $T_b$  as positive constants, while  $\sigma$ ,  $k$ , and  $Q$  are treated as piecewise constants.

Equation (2) can be formulated in a weak sense as we show below. First, we define the following Hilbert space:

$$V(\Omega) = \{v \in H^1(\Omega) : v = 0 \text{ on } \Gamma_b\}, \quad (4)$$

where the equality on  $\Gamma_b$  is understood in the sense of the traces [Eva10, Sec. 5.5] and we consider the following bilinear and linear form defined by:

$$\begin{aligned} a^\dagger(u, v) &:= \int_{\Omega} \sigma \nabla u \cdot \nabla v \, dx + \int_{\Omega} kuv \, dx + \int_{\Gamma_u} \alpha uv \, ds, \quad u, v \in H^1(\Omega), \\ l^\dagger(v) &:= \int_{\Omega} Qv \, dx + \int_{\Gamma_u} \alpha T_a v \, ds, \quad v \in H^1(\Omega). \end{aligned}$$

Next, we suppose that  $u_b \in H^1(\Omega)$  is such that  $u_b = T_b$  on  $\Gamma_b$ . Then, we obtain the weak formulation:

**Problem 2.2.** *Find  $u \in H^1(\Omega)$  such that*

$$\begin{cases} u = u_b + w, & w \in V(\Omega), \\ a^\dagger(w, v) = l^\dagger(v) - a^\dagger(u_b, v), & \forall v \in V(\Omega). \end{cases}$$

In Problem 2.2, it can be simply assumed that  $u_b \equiv T_b$  in  $\Omega$ , which expresses the weak formulation in the following manner: Find  $u \in V(\Omega)$  such that

$$a^\dagger(u, v) = l_b^\dagger(v), \quad \forall v \in V(\Omega),$$

where  $l_b^\dagger(v) = l^\dagger(v) - a^\dagger(T_b, v)$ . Clearly, when  $T_b \equiv 0$  in  $\bar{\Omega}$ , the linear form  $l_b^\dagger$  is exactly  $l^\dagger$ .

Hereinafter, we assume, unless otherwise specified, that  $T_b \equiv 0$  to simplify the arguments and notation, while retaining  $T_b$  in the formulations.

### 3. THE INVERSE PROBLEM

According to [Law56, LC63, BM<sup>+</sup>09], highly vascularized tumors can increase local blood flow and heat production, raising the temperature of the skin surface. This abnormal temperature can help predict the location and size of the tumor. To achieve this, the following inverse problem is solved:

**Problem 3.1.** *Given  $\Omega$ , constants  $T_a$ ,  $T_b$ ,  $\alpha$ , and a measured temperature profile  $h$  on the upper boundary  $\Gamma_u$ , find a subdomain  $\Omega_0^* \subset \Omega$  such that the solution  $u(\Omega_0^*)$  of the boundary value problem (2) with  $\Omega_0 = \Omega_0^*$  matches  $h$  on  $\Gamma_u$ ; i.e.,  $u|_{\Gamma_u} = h$  where  $u$  solves (2) with  $\Omega_0 = \Omega_0^*$ .*

For clarity, we emphasize here that all coefficients in (2), the data  $Q$ ,  $T_a$ ,  $T_b$ , and  $\partial\Omega$  are known parameters.

The straightforward way to find the *exact* inclusion  $\Omega_0^*$  is by minimizing the least-squares misfit function:

$$J_{LS}(\Omega_0, u(\Omega_0)) = \frac{1}{2} \int_{\Gamma_u} (u(\Omega_0) - h)^2 \, ds, \quad (5)$$

where  $J_{LS}$  reaches its minimum when  $\Omega_0 = \Omega_0^*$  (see [APT11]). To find the optimal shape solution of this functional, one applies shape sensitivity analysis [DZ11, HP18, MS76, SZ92], which examines the variation of the functional with respect to the unknown shape.

Since we will use tools from shape calculus, we must precisely define the admissible set of geometries for the inclusion  $\Omega_0$ . Let  $d_o > 0$  and define  $\Omega_o \Subset \Omega$  with a  $C^\infty$  boundary as:

$$\Omega_o := \{x \in \Omega \mid d(x, \partial\Omega) \geq d_o\}.$$

For  $k \in \mathbb{N}$ , we define the set of all admissible geometries or simply *hold-all* set  $U^k$  as follows:

$$U^k := \{\Omega_0 \in \Omega_o \mid d(x, \partial\Omega) > d_o, \forall x \in \Omega_0, \Omega_1 \text{ is connected, and } \Omega_0 \text{ is of class } C^{k,1}\}. \quad (6)$$

We say  $\Omega$  is *admissible* if it contains a subdomain  $\Omega_0 \in U^k$ . Hereinafter, without further notice, we assume that  $\Omega$  is admissible. Moreover, we assume the following key assumption:

**Assumption 3.2.** *There exists  $\Omega_0^* \in U^k$  such that  $u^* = u((\Omega_1 \setminus \overline{\Omega_0^*}) \cup \Omega_0^*)$  solves Problem 3.1.*

To emphasize the dependency of  $u$  on the inclusion  $\Omega_0$ , we will use the notation  $u(\Omega_0)$  instead of  $u((\Omega_1 \setminus \overline{\Omega_0}) \cup \Omega_0)$  for simplicity. Note that the mapping  $\Omega(\Omega_0) \mapsto u(\Omega(\Omega_0))$  is well-defined since Problem 2.2 is well-posed. Thus, we adopt the simplified notation  $J(\Omega_0) = J(\Omega_0, u(\Omega_0))$  for the functional  $J$ . Nonetheless, either notation is used when convenient.

#### 4. THE COUPLED COMPLEX BOUNDARY METHOD

In this study, we propose the Coupled Complex Boundary Method (CCBM) for shape optimization to numerically approximate the solution to the inverse problem. In the standard approach, the data needed for fitting, as described in (5), is collected from part or all of the accessible boundary or surface of the medium or object. However, this approach often leads to numerical instability, especially when tracking Neumann data using the least-squares method. In contrast, CCBM transfers the fitting data from the boundary to the interior of the domain, similar to the Kohn-Vogelius method [KV87]. For a Cauchy pair on the boundary subjected to measurement, CCBM achieves this by coupling Neumann and Dirichlet data to derive a Robin condition. Neumann and Dirichlet data represent the real and imaginary parts of the Robin boundary condition, respectively. This approach has a regularizing effect similar to that observed with the Kohn-Vogelius method [Rab23a]. Note, however, that this new boundary value problem is more complex and increases the dimension of the discrete system. Despite this, CCBM is more robust than the conventional misfit functional approaches, which rely on boundary integrals. Effective numerical methods can be developed within this framework.

Because measurements are only available on  $\Gamma_u \subsetneq \partial\Omega$ , the Kohn-Vogelius method does not yield a simple form for the cost functional, which defines the difference between two auxiliary problems. These problems involve the solutions of two PDEs: one with Dirichlet data and the other with corresponding Neumann data; see, e.g., [AR25, EH12]. Additionally, for Problem 3.1, the coupling is done using a Robin boundary condition and a Dirichlet data derived from measurements.

**4.1. The CCBM and contribution to the literature.** Initially introduced by Cheng et al. in [CGHZ14] for an inverse source problem, CCBM has been applied to various inverse problems. Gong et al. used it for an inverse conductivity problem in [GCH17], and Cheng et al. for parameter identification in elliptic problems in [ZCG20]. Afrates extended CCBM to shape inverse problems in [Afr22] and geometric inverse source problems in [AMN22]. It was later applied by the author for the exterior Bernoulli problem in [Rab23b], and by Rabago-Notsu for free surface problems in [RN24]. Ouiassa et al. used it for an inverse Cauchy Stokes problem in [OCNN22], and Rabago-Afrates-Notsu for detecting an immersed obstacle in Stokes fluid flow in [RAN25].

In this study, we use CCBM to locate a tumor in healthy tissue via thermal imaging based on Pennes' equation. Our approach is novel in formulating a domain integral cost functional with a single pair of Cauchy data on the accessible boundary. In free boundary [Rab23b] and free surface problems [RN24], CCBM has shown greater stability and accuracy than the classical least-squares approach, with computational cost similar to the Kohn-Vogelius method.

This study makes several contributions to the literature:

- We introduce a new cost functional (13) for addressing Problem 3.1, derived from the CCBM formulation; see subsection 4.2. This functional has not been previously studied in the context of the current problem.
- We derive the first-order shape derivative of the cost functional using Delfour-Zolésio's minimax formulation approach [DZ88]. To the best of our knowledge, this is the first

work to consider a Lagrangian formulation of an optimal control problem with a complex PDE constraint. We emphasize that the construction of the Lagrangian functional must be done carefully to obtain the correct expression. The method naturally applies to broader shape optimization problems constrained by complex-valued PDEs.

To compare our study with previous work, we begin by discussing the implementation of the approach (5) in [APT11]. In that study, the authors employed a second-order finite difference scheme to solve (2) for both the primal and adjoint systems. Focusing on the localization of melanoma nodules, they assumed the tumor to be circular, requiring only the center coordinates and radius for the inversion procedure. This simplification reduced the dimensionality of the design space for optimizing  $J_{LS}$ , as the design variables were limited to the tumor's center and radius. In contrast, the earlier work [PM07] identified the tumor region using an evolutionary algorithm combined with the multiple reciprocity boundary element method.

Our numerical approach differs from previous works in four key aspects:

- In contrast to [APT11], we employ FEMs to numerically solve the state and adjoint state equations. The design variables in our approach are the nodal points on the boundary interface.
- In the computation of the deformation fields, we use the volume integral representation of the shape gradient instead of the boundary integral form (see Hadamard-Zolèsio structure theorem [DZ11, Thm 3.6, p. 479]). For a comparison of the convergence order of volume and boundary formulations in the finite element framework, we refer the reader to [HPS15].
- Whereas [APT11] tests the numerical approach only in two dimensions, our work extends the methodology to three dimensions, thereby enhancing its applicability to higher-dimensional problems.
- To handle noisy measurements, we apply  $\rho$ -weighted volume penalization together with the *balancing principle* [CJK10b]. Originally developed for parameter identification, this principle is, to the best of our knowledge, applied here for the first time to a shape identification problem. The motivation and advantages of this approach, along with the Sobolev gradient method, are discussed in subsections 9.7 and 9.8. Additionally, we note that this approach avoids the need to calculate the curvature expression, which arises when using perimeter or surface measure penalization, as their shape derivatives involve curvature. While curvature is easy to compute in 2D, it is more complex in 3D.

Additionally, a mesh sensitivity analysis is carried out for the FE solution of the *material derivative* of the state problem; see Section 7. The goal is to demonstrate how the FE solution continuously depends on the mesh. To the best of the author's knowledge, this study is the first to conduct such an analysis, particularly in the context of numerical shape optimization problems solved using the Lagrangian method. The analysis builds on the ideas developed in [HH21] on mesh sensitivity analysis for FE solutions of linear elliptic PDEs.

Some remarks on the choice of shape gradient structure are necessary.

**Remark 4.1.** *As already mentioned, shape gradients of PDE-constrained functionals can be expressed in two equivalent ways. Both typically involve solving two boundary value problems (BVPs), but one integrates their traces on the domain boundary, while the other evaluates volume integrals. When these BVPs are solved approximately using, for example, FEMs, the equivalence of the two formulas no longer holds. [HPS15] analyzed volume and boundary formulations, demonstrating through convergence analysis and numerical experiments that the volume-based expression generally provides greater accuracy in a finite element setting. Following the aforementioned work, numerous studies have explored this direction. We provide a non-exhaustive list of research examining various objective functionals constrained by PDEs, including the elliptic PDEs, the Stokes equation, the Navier-Stokes equation, etc: [EHLW20, GLR24, GLZ22, GZ21, LS16, Lau20, LZ19, LZ22, LZ23, LZS23, Pag14, PH16, Zhu18].*

**4.2. The CCBM formulation.** The CCBM formulation of Problem 3.1 is similar to (2), except that on the measurement region  $\Gamma_u$ , the boundary condition is:

$$-\sigma_1 \frac{\partial u_1}{\partial n} - iu_1 = \alpha(u_1 - T_a) - ih, \quad \text{on } \Gamma_u.$$

where  $i = \sqrt{-1}$  and  $h$  is the measured data on  $\Gamma_u$ . In the rest of the paper, we refer to (2) with this boundary condition as the *CCBM equation*.

Let  $u = u^r + iu^i : \Omega \rightarrow \mathbb{C}$  be a solution of the CCBM equation. Then, the real-valued functions  $u^r : \Omega \rightarrow \mathbb{R}$  and  $u^i : \Omega \rightarrow \mathbb{R}$  satisfy the following systems of real PDEs:

$$\left\{ \begin{array}{ll} -\sigma_1 \Delta u_1^r + k_1 u_1^r = Q_1, & \text{in } \Omega_1, \\ -\sigma_0 \Delta u_0^r + k_0 u_0^r = Q_0, & \text{in } \Omega_0, \\ u_1^r = u_0^r, & \text{on } \partial\Omega_0, \\ -\sigma_1 \frac{\partial u_1^r}{\partial n} = -\sigma_0 \frac{\partial u_0^r}{\partial n}, & \text{on } \partial\Omega_0, \quad (7) \\ -\sigma_1 \frac{\partial u_1^r}{\partial n} = \alpha(u_1^r - T_a) - u_1^i, & \text{on } \Gamma_u, \\ -\sigma_1 \frac{\partial u_1^r}{\partial n} = 0, & \text{on } \Gamma_w, \\ u_1^r = T_b, & \text{on } \Gamma_b, \end{array} \right. \quad \left\{ \begin{array}{ll} -\sigma_1 \Delta u_1^i + k_1 u_1^i = 0, & \text{in } \Omega_1, \\ -\sigma_0 \Delta u_0^i + k_0 u_0^i = 0, & \text{in } \Omega_0, \\ u_1^i = u_0^i, & \text{on } \partial\Omega_0, \\ -\sigma_1 \frac{\partial u_1^i}{\partial n} = -\sigma_0 \frac{\partial u_0^i}{\partial n}, & \text{on } \partial\Omega_0, \quad (8) \\ -\sigma_1 \frac{\partial u_1^i}{\partial n} = \alpha u_1^i - h + u_1^r, & \text{on } \Gamma_u, \\ -\sigma_1 \frac{\partial u_1^i}{\partial n} = 0, & \text{on } \Gamma_w, \\ u_1^i = 0, & \text{on } \Gamma_b. \end{array} \right.$$

**Remark 4.2.** If  $u^i = u_1^i + iu_0^i = 0$  in  $\Omega$ , then  $[u^i] = [\sigma \partial_n u^i] = 0$  on  $\partial\Omega_0$ . On  $\Gamma_b$ ,  $\partial_n u_1^i = 0$ . Similarly, on  $\Gamma_w$ ,  $u_1^i = 0$  since  $\sigma_1 > 0$ . Thus,  $u_1^i = 0$  on  $\Gamma_b \cup \Gamma_w \cup \partial\Omega_0$ .

Considering the variational equation:

$$\int_{\Gamma_u} \sigma_1 \partial_n u_1^i \varphi \, ds = \int_{\partial\Omega_1} \sigma_1 \partial_n u_1^i \varphi \, ds = \int_{\Omega_1} (\sigma_1 \nabla u_1^i \cdot \nabla \varphi + k_1 u_1^i \varphi) \, dx = 0, \quad \forall \varphi \in V(\Omega). \quad (9)$$

Clearly,  $\partial_n u_1^i = 0$  on  $\Gamma_u$ , so  $u_1^i = 0$  on  $\Gamma_u$ . Note that, if we suppose that  $\partial_n u_1^i \neq 0$  on  $\Gamma_u$ , then  $u_1^i \neq 0$  on  $\Gamma_u$ . Taking  $\varphi = u_1^i \in V(\Omega)$  as the test function in (9) leads to a contradiction. Hence,  $h - u_1^r = \sigma_1 \frac{\partial u_1^i}{\partial n} + \alpha u_1^i = 0$  on  $\Gamma_u$ , or equivalently,  $u_1^r = h$  on  $\Gamma_u$ . Therefore, from PDEs (7) and (8),  $(\Omega_0, u^r)$  solves Problem 3.1. Conversely, if  $(\Omega_0, u)$  solves Problem 3.1, then it satisfies the CCBM equation.

Remark 4.2 implies that Problem 3.1 can equivalently be formulated as follows:

**Problem 4.3.** Find  $\Omega_0 \in U^k$ ,  $k \in \mathbb{N}$ , such that  $u^i \equiv 0$  in  $\Omega$ , where  $u$  satisfy the CCBM equation.

**4.3. Well-posedness of the CCBM equation.** For functions  $\varphi, \psi : \Omega \rightarrow \mathbb{C}$  on the complex Sobolev space  $V(\Omega) := \{\varphi = \varphi^r + i\varphi^i \in H^1(\Omega) \mid \varphi^r = \varphi^i = 0 \text{ on } \Gamma_b\}$ , we define the following sesquilinear and linear forms:

$$\begin{aligned} a(\varphi, \psi) &:= \int_{\Omega} (\sigma \nabla \varphi \cdot \nabla \bar{\psi} + k\varphi \bar{\psi}) \, dx + \int_{\Gamma_u} (\alpha + i)\varphi \bar{\psi} \, ds, \\ l(\psi) &:= \int_{\Omega} Q \bar{\psi} \, dx + \alpha \int_{\Gamma_u} T_a \bar{\psi} \, ds + i \int_{\Gamma_u} h \bar{\psi} \, ds, \end{aligned} \quad (10)$$

where  $T_a \in H^{-1/2}(\Gamma_u)$ .

The weak form of the CCBM equation can be stated as follows:

**Problem 4.4.** Find  $u \in H^1(\Omega)$  such that

$$a(\varphi, \psi) = l(\psi), \quad \forall \psi \in V(\Omega).$$

The solution to Problem 4.4 will henceforth be called the *state solution*. The following result establishes the well-posedness of the weak formulation.



**Proposition 4.5.** *Let  $\Omega$  be a Lipschitz bounded domain,  $\alpha \in \mathbb{R}_+$ ,  $Q \in H^{-1}(\Omega)$ ,  $T_a \in H^{-1/2}(\Gamma_u)$ ,  $h \in H^{1/2}(\Gamma_u)$ , and the known parameters be given such that Assumption 2.1 holds. Then, Problem 4.4 admits a unique weak solution  $u \in V(\Omega)$  which continuously depends on the data  $Q$ ,  $T_a$ , and  $h$ . Moreover,*

$$\|u\|_{1,\Omega} \leq c_0 \left( \|Q\|_{H^{-1}(\Omega)} + \|T_a\|_{H^{-1/2}(\Gamma_u)} + \|h\|_{H^{1/2}(\Gamma_u)} \right), \quad (11)$$

where  $c_0 > 0$  depends on  $\alpha$ ,  $\underline{\sigma}$ , and  $\underline{k}$ .

*Proof.* The assertion follows from standard arguments (see, e.g., the proof of [CGHZ14, Prop. 2.2]). Specifically, the conclusion is inferred from the complex version of the Lax-Milgram lemma [DL98, p. 376] by demonstrating that the sesquilinear form  $a(\cdot, \cdot)$  is continuous and coercive on  $V(\Omega)$ , and the linear form  $l(\cdot)$  is continuous on  $V(\Omega)$  ([DL98, Def. 4, p. 368]). That is, there exists a constant  $c_1 > 0$  such that

$$\Re a(u, u) \geq c_1 \|u\|_{1,\Omega}^2, \quad \forall u \in V(\Omega). \quad (12)$$

The proof of coercivity uses bounds on the coefficients  $\sigma$  and  $k$ ; i.e.,  $c_1 = c_1(\underline{\sigma}, \underline{k})$ . The proof is omitted.  $\square$

In Proposition 4.5, we see that it is sufficient to assume lower regularity for  $\Omega$ ,  $Q$ ,  $T_a$ , and  $h$  than what is specified in Assumption 2.1. Additionally,  $T_a$  is considered non-constant. Moving forward, we will adopt the regularity outlined in Assumption 2.1 since a higher regularity of the state solution is necessary. Moreover, unless otherwise specified,  $T_a \in \mathbb{R}_+$ .

**4.4. The shape optimization formulation.** From Proposition 4.5, we know that the state problem is uniquely solvable in  $V(\Omega)$ . Consequently, for any  $\Omega_0 \in U^1$ , we can define the map  $\Omega(\Omega_0) \mapsto u(\Omega(\Omega_0))$ . This allows us to consider, in view of Remark 4.2, minimizing the following shape functional to solve Problem 4.3:

$$J(\Omega_0) := \frac{1}{2} \int_{\Omega} (u^i)^2 dx. \quad (13)$$

We then pose the minimization problem:

**Problem 4.6.** *Let  $\Omega$  be admissible. Find  $\Omega_0^* \in U^1$  such that*

$$\Omega_0^* = \operatorname{argmin}_{\Omega_0 \in U^1} J(\Omega_0).$$

**Remark 4.7.** *The new method allows us to define the cost function  $J$  in the entire domain  $\Omega$ , which brings advantages in terms of robustness in the reconstruction, such as the Kohn-Vogelius cost functional [KV87], compared to the least-squares misfit functional  $J_{LS}$ , which is defined only on the subboundary  $\Gamma_u$ ; see (5).*

## 5. SHAPE SENSITIVITY ANALYSIS

**5.1. Some concepts from shape calculus.** We consider specific deformations of  $\Omega_0$  through a set of admissible deformation fields, which we define as follows:

$$\Theta^k := \{\theta \in C^{k,1}(\mathbb{R}^d) \mid \operatorname{supp} \theta \subset \bar{\Omega}_o\}. \quad (14)$$

For  $\theta \in \Theta^k$ , we denote  $\theta_n := \langle \theta, n \rangle$ .

We define the transformation  $T_t : \bar{\Omega} \rightarrow \bar{\Omega}$  as  $T_t = I + t\theta$ , where  $\theta \in \Theta^k$ . Accordingly, we define  $\Omega_{0,t} := T_t(\Omega_0)$ ,  $\partial\Omega_{0,t} := T_t(\partial\Omega_0)$ ,  $\Omega_{1,t} := T_t(\Omega_1)$ , and  $\partial\Omega_{1,t} := T_t(\partial\Omega_1)$ . In addition,  $\Omega_t = T_t(\Omega) = \Omega_{1,t} \cup \bar{\Omega}_{0,t}$  and  $\partial\Omega_t = \partial\Omega$  since  $\theta|_{\partial\Omega} = 0$ . We refer to a function  $\varphi_t : \Omega_t \rightarrow \mathbb{R}$  on the reference domain  $\Omega$  using  $T_t$ , denoting  $\varphi^t := \varphi_t \circ T_t : \Omega \rightarrow \mathbb{R}$ .

We let  $t_0 > 0$  be such that, for all  $t \in \mathcal{I} := [0, t_0)$ ,  $T_t$  becomes a  $C^{k,1}$  diffeomorphism from  $\Omega$  onto its image (cf. [BP13, Thm. 7] for  $k = 1$ ). Hereinafter, we assume that  $t \in \mathcal{I}$  unless stated otherwise.

The set of all admissible perturbations of  $\Omega_0$ , denoted here by  $\Upsilon^k$ , is defined as:

$$\Upsilon^k = \left\{ T_t(\theta)(\bar{\Omega}_0) \subset \Omega \mid \Omega_0 \in U^k, t \in \mathcal{I}, \theta \in \Theta^k \right\}. \quad (15)$$

The fixed boundary  $\partial\Omega$  does not need  $C^{k,1}$  regularity; Lipschitz continuity suffices. Nevertheless, higher regularity is assumed here for simplicity.

The following regularities hold (see, e.g., [IKP06, IKP08] or [SZ92, Lem. 3.2, p. 111]):

$$\left\{ \begin{array}{ll} [t \mapsto DT_t] \in C^1(\mathbb{I}, C^{0,1}(\bar{\Omega})^{d \times d}), & [t \mapsto (DT_t)^{-\top}] \in C^1(\mathbb{I}, C(\bar{\Omega})^{d \times d}), \\ [t \mapsto I_t] \in C^1(\mathbb{I}, C(\bar{\Omega})), & [t \mapsto I_t := \det DT_t] \in C^1(\mathbb{I}, C^{0,1}(\bar{\Omega})), \\ [t \mapsto A_t] \in C^1(\mathbb{I}, C(\bar{\Omega})^{d \times d}), & [t \mapsto A_t := I_t M_t^\top M_t] \in C(\mathbb{I}, C(\bar{\Omega})^{d \times d}), \\ [t \mapsto b_t := I_t |M_t n|] \in C^1(\mathbb{I}, C(\partial\omega)), & M_t := (DT_t)^{-\top}. \end{array} \right. \quad (16)$$

The derivatives of the maps  $[t \mapsto I_t]$ ,  $[t \mapsto A_t]$ , and  $[t \mapsto b_t]$  are given by:

$$\begin{aligned} \frac{d}{dt} I_t \Big|_{t=0} &= \lim_{t \rightarrow 0} \frac{I_t - 1}{t} = \operatorname{div} \theta, \\ \frac{d}{dt} A_t \Big|_{t=0} &= \lim_{t \rightarrow 0} \frac{A_t - I}{t} = (\operatorname{div} \theta)I - D\theta - (D\theta)^\top =: A, \\ \frac{d}{dt} b_t \Big|_{t=0} &= \lim_{t \rightarrow 0} \frac{b_t - 1}{t} = \operatorname{div}_\tau \theta = \operatorname{div} \theta \Big|_\tau - (D\theta n) \cdot n. \end{aligned} \quad (17)$$

Taking smaller interval  $\mathbb{I}$  if necessary, we assume here that

$$|\xi|^2 \leq \sigma A_t \xi \cdot \xi \leq |\xi|^2, \quad \forall \xi \in \mathbb{R}^d. \quad (18)$$

The functional  $J : \Upsilon^k \rightarrow \mathbb{R}$  has a directional first-order Eulerian derivative at  $\Omega$  in the direction  $\theta \in \Theta^k$  if the limit

$$\lim_{t \searrow 0} \frac{J(\Omega_{0,t}) - J(\Omega_0)}{t} =: dJ(\Omega_0)[\theta] \quad (19)$$

exists [DZ11, Sec. 4.3.2, Eq. (3.6), p. 172]. We say  $J$  is shape differentiable at  $\Omega_0$  if the mapping  $\theta \mapsto dJ(\Omega_0)[\theta]$  is linear and continuous in  $C^{k,1}(\bar{\Omega})^d$ , for some  $k \in \mathbb{N} \cup \{0\}$ . The resulting map is called the *shape gradient* of  $J$ .

**5.2. Shape derivative of the cost.** Let us introduce the sesquilinear form  $a_{\text{adj}}(\cdot, \cdot)$ :

$$a_{\text{adj}}(\varphi, \psi) := \int_\Omega (\sigma \nabla \varphi \cdot \nabla \bar{\psi} + k \varphi \bar{\psi}) dx + \alpha \int_{\Gamma_u} \varphi \bar{\psi} ds - i \int_{\Gamma_u} \varphi \bar{\psi} ds, \quad \varphi, \psi \in V(\Omega). \quad (20)$$

The main result of this section is the shape derivative of the cost function  $J$  given in the following theorem.

**Theorem 5.1.** *Let Assumption 2.1 holds. Assume  $\Omega$  is an admissible domain and  $\theta$  an admissible deformation field. Then,  $J$  is shape differentiable, and its distributed shape derivative  $dJ(\Omega_0)[\theta]$  is given by*

$$\begin{aligned} dJ(\Omega_0)[\theta] &= \frac{1}{2} \int_\Omega \operatorname{div} \theta u^i{}^2 dx - \int_\Omega \operatorname{div} \theta \sigma \sum_{j=1}^d (\partial_j u^i \partial_j p^r - \partial_j u^r \partial_j p^i) dx \\ &\quad + \int_\Omega \sigma \sum_{m=1}^d \sum_{j=1}^d \partial_j \theta_m (\partial_j u^i \partial_m p^r - \partial_j u^r \partial_m p^i) dx \\ &\quad + \int_\Omega \sigma \sum_{m=1}^d \sum_{j=1}^d \partial_j \theta_m (\partial_m u^i \partial_j p^r - \partial_m u^r \partial_j p^i) dx \\ &\quad + \int_\Omega \operatorname{div} \theta k (u^i p^r - u^r p^i) dx + \int_\Omega \operatorname{div} \theta Q p^i dx, \end{aligned} \quad (21)$$

where  $A$  is given in (17),  $u$  is the state solution, and  $p \in V(\Omega)$  is the adjoint variable solving:

$$a_{\text{adj}}(p, v) = \int_\Omega u^i \bar{v} dx, \quad \forall v \in V(\Omega). \quad (22)$$

**Remark 5.2** (Construction of the Lagrangian functional). *In the minimax formulation, constructing the Lagrangian functional is crucial. In optimal control problems with real PDE constraints, the application is straightforward [Stu16], as it involves the sum of a utility function and equality constraints. However, in this work, careful construction of the Lagrangian is necessary due to the complex nature of the PDE constraints.*

To illustrate how the Lagrangian functional should be constructed, we provide the following formal computation of the directional derivative of  $J$  in the direction of an arbitrary function  $v \in V(\Omega)$ :

$$\begin{aligned}
 J'(u(\Omega))[v(\Omega)] &= \left. \frac{d}{d\varepsilon} \{J(u(\Omega) + \varepsilon v(\Omega))\} \right|_{\varepsilon=0} \\
 &= \left. \frac{d}{d\varepsilon} \left\{ \frac{1}{2} \int_{\Omega} (u^i + \varepsilon \Im\{v\})^2 dx \right\} \right|_{\varepsilon=0} \\
 &= \left. \left\{ \int_{\Omega} (u^i + \varepsilon \Im\{v\}) \Im\{v\} dx \right\} \right|_{\varepsilon=0} \\
 &= \int_{\Omega} u^i \Im\{v\} dx \\
 &= \Im \left\{ \int_{\Omega} u^i v dx \right\}.
 \end{aligned} \tag{23}$$

Suppose  $F(t, \varphi, \psi)$  denotes the Lagrangian functional associated with the CCBM formulation. Assume  $F$  is sufficiently differentiable with respect to  $t$ ,  $\phi$ , and  $\psi$ , and the strong material derivative  $\dot{u}$  exists in  $V(\Omega)$ . We can then compute:

$$dJ(\Omega_0)[\theta] = \left. \frac{d}{dt} F(t, u_t, p) \right|_{t=0} = \underbrace{\left. \frac{\partial F}{\partial t}(t, u, p) \right|_{t=0}}_{\text{shape derivative}} + \underbrace{\left. \frac{\partial F}{\partial \phi}(0, u, p)(\dot{u}) \right|_{t=0}}_{\text{adjoint equation}}. \tag{24}$$

Since  $\dot{u} \in V(\Omega)$ , it follows that:

$$dJ(\Omega_0)[\theta] = \left. \frac{\partial F}{\partial t}(t, u, p) \right|_{t=0}.$$

Now, taking the complex conjugate of both sides of (67), we obtain:

$$\overline{a_{adj}(p, v)} = \int_{\Omega} (\sigma \nabla \bar{p} \cdot \nabla v + k \bar{p} v) dx + \int_{\Gamma_u} (\alpha + i) \bar{p} v ds = \int_{\Omega} u^i v dx. \tag{25}$$

Thus, to ensure consistency between (23), (24), and (25), the imaginary part of the equality constraint, corresponding to the adjoint equation, must be taken in the intermediate computation of the shape derivative using the minimax formulation.

We derive the shape derivative of  $J$  (i.e., the proof of Theorem 5.1) via minimax formulation in the spirit of [DZ88]. This method enables us to find the derivative of the shape functional without computing the material or shape derivative of the state. An alternative is the rearrangement method developed in [IKP08, IKP06], which avoids such computation. To proceed, we introduce the Lagrangian functional

$$L(\Omega_0, \varphi, \psi) := J(\Omega_0, \varphi) + \Im \{l(\psi) - a(\varphi, \psi)\}, \quad \varphi, \psi \in V(\Omega),$$

where  $a$  and  $l$  are given in (10) while  $\Im \{\cdot\}$  denotes the imaginary part. Observe that

$$J(\Omega_0, u(\Omega_0)) = \min_{\varphi \in V(\Omega)} \sup_{\psi \in V(\Omega)} L(\Omega_0, \varphi, \psi),$$

because

$$\sup_{\psi \in V(\Omega)} L(\Omega_0, \varphi, \psi) = \begin{cases} J(\Omega_0, u(\Omega_0)) & \text{if } \varphi = u \in V(\Omega), \\ +\infty & \text{otherwise.} \end{cases}$$

It can be verified that  $L$  is convex and continuous with respect to  $\varphi$  and concave and continuous with respect to  $\psi$  (cf. [Rab23a]). Thus, by Ekeland and Temam [ET76],  $L$  has a saddle point  $(u, p) \in V(\Omega)^2$  if and only if  $(u, p) \in V(\Omega)^2$  satisfies the system:

$$\begin{cases} \left. \frac{\partial}{\partial \varphi} L(\Omega_0, \varphi, \psi)[v] \right|_{(\varphi, \psi)=(u, p)} = 0, & v \in V(\Omega), \\ \left. \frac{\partial}{\partial \psi} L(\Omega_0, \varphi, \psi)[v] \right|_{(\varphi, \psi)=(u, p)} = 0, & v \in V(\Omega). \end{cases} \quad (26)$$

The first equation corresponds to the variational equation of the state problem, while the second characterizes the adjoint solution.

An analogous Lagrangian functional can be defined over the perturbed domain, and the previous analysis still applies. Specifically, we have the following expression:

$$J(\Omega_{0,t}, u(\Omega_{0,t})) = \min_{\varphi \in V(\Omega_t)} \sup_{\psi \in V(\Omega_t)} L(\Omega_{0,t}, \varphi, \psi), \quad (27)$$

with the corresponding saddle point characterized by the following system of PDEs:

$$\begin{cases} \left. \frac{\partial}{\partial \varphi} L(\Omega_{0,t}, \varphi, \psi)[v] \right|_{(\varphi, \psi)=(u(\Omega_{0,t}), p(\Omega_{0,t}))} = 0, & v \in V(\Omega_t), \\ \left. \frac{\partial}{\partial \psi} L(\Omega_{0,t}, \varphi, \psi)[v] \right|_{(\varphi, \psi)=(u(\Omega_{0,t}), p(\Omega_{0,t}))} = 0, & v \in V(\Omega_t). \end{cases} \quad (28)$$

The main steps for the remainder of the proof are as follows:

- we differentiate  $L(\Omega_{0,t}, \varphi, \psi)$  with respect to  $t \geq 0$ ; i.e., we evaluate (19) by using (27);
- we verify the assumptions of Correa-Seeger Theorem [CS85].

To derive  $L(\Omega_{0,t}, \varphi, \psi)$  with respect to  $t \geq 0$ , we apply Theorem A.1 ([CS85]). To achieve this, the domain  $\Omega_{0,t}$  must be mapped back to the reference domain  $\Omega_0$  using the transformation  $T_t$ . However, composing by  $T_t$  inside the integrals results in terms  $u \circ T_t$  and  $p \circ T_t$ , which could be non-differentiable. To address this, we parameterize  $H^1(\Omega)$  by composing its elements with  $T_t^{-1}$ . Thus, we write

$$F(t, \varphi, \psi) := L(\Omega_{0,t}, \varphi \circ T_t^{-1}, \psi \circ T_t^{-1}).$$

After applying a change of variables, we obtain

$$F(t, \varphi, \psi) = \frac{1}{2} \int_{\Omega} I_t \varphi^2 dx - \mathfrak{S} \left\{ \int_{\Omega} (\sigma^t A_t \nabla \varphi \cdot \nabla \bar{\psi} + I_t k^t \varphi \bar{\psi}) dx + \int_{\Gamma_u} (\alpha + i) b_t \varphi \bar{\psi} ds - \int_{\Omega} I_t Q^t \bar{\psi} dx - \alpha \int_{\Gamma_u} b_t T_a^t \bar{\psi} ds - i \int_{\Gamma_u} b_t h^t \bar{\psi} ds \right\}.$$

On  $\partial\Omega$ , we note that  $b_t = 1$  for all  $t > 0$  since  $\theta|_{\partial\Omega} = 0$ . In view of (28),  $F$  has a unique saddle point  $(u^t, p^t) \in V(\Omega)^2$  for all  $t \in \mathfrak{l}$ , satisfying the system of PDEs

$$\begin{cases} \int_{\Omega} (\sigma^t A_t \nabla u^t \cdot \nabla v + I_t k^t u^t v) dx + \int_{\Gamma_u} (\alpha + i) b_t u^t \bar{v} ds - \int_{\Omega} I_t Q^t \bar{v} dx - \alpha \int_{\Gamma_u} b_t T_a^t \bar{v} ds - i \int_{\Gamma_u} b_t h^t \bar{v} ds = 0, & \forall v \in V(\Omega) \\ \int_{\Omega} (\sigma^t A_t \nabla p^t \cdot \nabla \bar{v} + I_t k^t p^t \bar{v}) dx - i \int_{\Gamma_u} b_t p^t \bar{v} ds + \int_{\Omega} I_t u_1^t \bar{v} dx = 0, & \forall v \in V(\Omega). \end{cases} \quad (29)$$

Since the assumptions of Theorem A.1 are satisfied (see next subsection), we obtain

$$\begin{aligned}
 dJ(\Omega_0)[\theta] &= \partial_t F(t, u, p)|_{t=0} \\
 &= \frac{1}{2} \int_{\Omega} \operatorname{div} \theta u^2 dx - \Im \left\{ \int_{\Omega} (\sigma A \nabla u \cdot \nabla \bar{p} + \operatorname{div} \theta k u \bar{p} - \operatorname{div} \theta Q \bar{p}) dx \right\} \\
 &\quad - \Im \left\{ \int_{\Omega} (\nabla \sigma \cdot \theta (\nabla u \cdot \nabla \bar{p}) + \nabla k \cdot \theta u \bar{p} - \theta \cdot \nabla Q) \bar{p} dx \right\} \\
 &= \frac{1}{2} \int_{\Omega} \operatorname{div} \theta u^2 dx - \Im \left\{ \int_{\Omega_1} (\sigma_1 A \nabla u_1 \cdot \nabla \bar{p}_1 + \operatorname{div} \theta k_1 u_1 \bar{p}_1 - \operatorname{div} \theta Q_1 \bar{p}_1) dx \right. \\
 &\quad + \int_{\Omega_0} (\sigma_0 A \nabla u_0 \cdot \nabla \bar{p}_0 + \operatorname{div} \theta k_0 u_0 \bar{p}_0 - \operatorname{div} \theta Q_0 \bar{p}_0) dx \\
 &\quad + \int_{\Omega_1} (\nabla \sigma_1 \cdot \theta (\nabla u_1 \cdot \nabla \bar{p}_1) + \nabla k_1 \cdot \theta u_1 \bar{p}_1 - \theta \cdot \nabla Q_1 \bar{p}_1) dx \\
 &\quad \left. + \int_{\Omega_0} (\nabla \sigma_0 \cdot \theta (\nabla u_0 \cdot \nabla \bar{p}_0) + \nabla k_0 \cdot \theta u_0 \bar{p}_0 - \theta \cdot \nabla Q_0 \bar{p}_0) dx \right\},
 \end{aligned}$$

which is, after taking the imaginary part of the expression inside the bracket leads to (21).

**5.3. Verifying the conditions of Correa-Seeger Theorem.** Let us verify the conditions of Theorem A.1 ([CS85]) following closely the discussion in [DZ11, Chap. 10.2, p. 521 and Chap. 10.5, p. 551]. For all  $t \in \mathbb{I}$ , we define

$$\begin{aligned}
 X(t) &:= \left\{ x^t \in V(\Omega) \mid \sup_{y \in V(\Omega)} F(t, x^t, y) = \min_{x \in V(\Omega)} \sup_{y \in V(\Omega)} F(t, x, y) \right\} \\
 Y(t) &:= \left\{ y^t \in V(\Omega) \mid \min_{x \in V(\Omega)} F(t, x, y^t) = \sup_{y \in V(\Omega)} \min_{x \in V(\Omega)} F(t, x, y) \right\}.
 \end{aligned}$$

Clearly, (H1) is satisfied because, for all  $t \in \mathbb{I}$ ,  $S(t) = X(t) \times Y(t)$  contains the pair  $(u^t, p^t)$  and is therefore non-empty. Assumption (H2) also holds since the map  $t \mapsto F(t, u^t, p^t)$  is differentiable on  $\mathbb{I}$ , thanks to the properties of the transformation  $T_t$  in (16) and (17), as well as the assumptions on the coefficients and data given in Assumption 2.1. To see this, we mimic the arguments used in [DZ11, Sec. 5.5, pp. 557-560]. Indeed, let us suppose that  $(u^t, p^t) \in V(\Omega) \times V(\Omega)$  is a saddle point of  $F(t, \varphi, \psi)$ . By definition, this implies the inequalities

$$F(t, u^t, \psi) \leq F(t, u^t, p^t) \leq F(t, \varphi, p^t),$$

for all  $\psi \in V(\Omega)$  and  $\varphi \in V(\Omega)$ . This further gives

$$F(t, u^t, p^t) \leq F(t, u, p^t) \quad \text{and} \quad F(0, u, p) \leq F(0, u^t, p).$$

Let  $\Delta(t) := F(t, u^t, p^t) - F(0, u, p)$ . Then,

$$F(t, u^t, p) - F(0, u^t, p) \leq \Delta(t) \leq F(t, u, p^t) - F(0, u, p^t).$$

Using the Mean Value Theorem, for each  $t \in \mathbb{I}$ , there exist constants  $c_t, \tilde{c}_t \in (0, 1)$  such that

$$t \partial_t F(t c_t, u^t, p) \leq \Delta(t) \leq t \partial_t F(t \tilde{c}_t, u, p^t). \quad (30)$$

It follows that the map  $(t, \varphi) \mapsto \partial_t F(t, \varphi, p)$  is strongly continuous, while  $(t, \psi) \mapsto \partial_t F(t, u, \psi)$  is weakly continuous. Furthermore, the mappings  $t \mapsto u^t$  and  $t \mapsto p^t$  are bounded in  $V$ , using (16), (17), and (18).

Now, for any sequence  $\{t_n\} \subset \mathbb{I}$  such that  $t_n \rightarrow 0$  as  $n \rightarrow \infty$ , we have

$$u^{t_n} \rightharpoonup u^0 \quad \text{and} \quad p^{t_n} \rightharpoonup p^0 \quad \text{in } V(\Omega) \quad (n \rightarrow \infty),$$

where  $(u^0, p^0) \in V(\Omega) \times V(\Omega)$ . Passing to the limit in (29) and using (16) and (17), we find that  $(u^0, p^0)$  solves (26); i.e., the equations hold with  $(\varphi, \psi) = (u^0, p^0)$ . By uniqueness,  $(u^0, p^0) = (u, p)$ , where  $u$  is the state solution and  $p \in V(\Omega)$  solves (67). Choosing a subsequence  $\{t_{n_k}\}$  (if necessary) ensures the required strong convergence in  $V$ . Hence, the strong continuity

of  $(t, u) \rightarrow \partial_t F(t, u, p)$  and  $(t, p) \rightarrow \partial_t F(t, u, p)$ . Therefore, (H3) and (H4) are also verified. From (30), we conclude that

$$\liminf_{t \searrow 0} \frac{1}{t} \Delta(t) \geq \partial_t F(0, u, p) \quad \text{and} \quad \limsup_{t \searrow 0} \frac{1}{t} \Delta(t) \leq \partial_t F(0, u, p).$$

Combining these yields

$$\limsup_{t \searrow 0} \frac{1}{t} \Delta(t) = \liminf_{t \searrow 0} \frac{1}{t} \Delta(t).$$

This completes the proof.

The following result can be easily drawn from (21) and (67).

**Corollary 5.3** (Necessary condition). *Let the subdomain  $\Omega_0^*$  be such that  $u = u(\Omega(\Omega_0^*))$  satisfies (2), i.e., there holds*

$$u^i \equiv 0 \quad \text{on } \Omega(\Omega_0^*). \quad (31)$$

*Then,  $\Omega_0^*$  is a stationary solution of Problem 4.3. That is, it fulfills the necessary optimality condition*

$$dJ(\Omega_0^*)[\theta] = 0, \quad \forall \theta \in \Theta^1. \quad (32)$$

*Proof.* Assuming that  $u^i \equiv 0$  in  $\Omega(\Omega_0^*)$ , it follows that  $p = 0$  in  $\Omega(\Omega_0^*)$ . Therefore, we have  $dJ(\Omega_0^*) \equiv 0$  in  $\Omega(\Omega_0^*)$ , which implies that  $dJ(\Omega_0^*)[\theta] = 0$  for all  $\theta \in \Theta^1$ .  $\square$

## 6. MESH DEFORMATION

Before presenting the numerical realization of the proposed method, we first analyze the sensitivity of the FE solution of the state problem to mesh variations. The main result, presented in Theorem 7.7, establishes a bound on the variation of the finite element solution in terms of the mesh deformation and its gradient. Additionally, a similar bound is provided in equation (65) for cases where the mesh velocity field is nonsmooth. These findings demonstrate the continuous dependence of the FE solution of the state problem on the mesh. The results apply to any dimension, arbitrary unstructured simplicial meshes, and broad classes of finite element approximations. Numerical illustrations are provided in subsection 9.4. Since this section largely follows the preparation in [HH21], we adopt the same notations used in the referenced paper. Most of the notations also follow those in [EG04]. For simplicity, we assume throughout this section (and also in Section 8) that  $\alpha \in \mathbb{R}_+$  and  $T_b = 0$  in  $\Gamma_b$ .

**6.1. Finite element formulation.** We consider the FE solution of Problem 4.4. To streamline the discussion, notation, and writing, we assume for simplicity that  $\sigma, k \in W^{1,\infty}(\Omega)$ ,  $Q \in H^1(\Omega)$ , and  $T_a, h \in H^{1/2}(\Gamma_u)$ . Note that these regularity assumptions enable us to achieve  $H^2$  regularity for the state  $u$ .

We begin by gathering some elements involved in the formulation. Let  $\mathcal{T}_h$  be a simplicial mesh triangulation of the domain  $\Omega$ , with  $K$  as a generic element of  $\mathcal{T}_h$ . We denote by  $h_K$  and  $a_K$  the diameter (i.e., the length of the longest side) and the minimum height of  $K$ , respectively. For later use, we label the vertices of  $K$  as  $x_0^K, \dots, x_d^K$ . Here, the height of  $K$  refers to the distance from a vertex to its opposite facet. The mesh  $\mathcal{T}_h$  is said to be a shape-regular triangulation of the domain  $\Omega$  if there a constant  $\bar{h} > 0$  such that

$$\frac{h_K}{a_K} \leq \bar{h}, \quad \forall K \in \mathcal{T}_h.$$

In the literature,  $\mathcal{T}_h$  is typically defined in terms of the mesh size  $h$ , given by  $h = \max_{K \in \mathcal{T}_h} h_K \equiv \max_{K \in \mathcal{T}_h} \max_{0 \leq i, j \leq d} |x_i - x_j|$ . Note that, in finite element error analysis, it is common to assume shape-regular meshes. However, in our current mesh sensitivity analysis, we do not impose this assumption. Instead, we only require each element to be *non-degenerate* (see, e.g., [BS08, Def. 4.4.13, eq. (4.4.16), p. 108]) or *non-inverted*, which is equivalent to requiring  $a_K > 0$  for all  $K \in \mathcal{T}_h$ .

In the latter part of this section, we discuss key tools in our analysis related to the properties of the mesh element  $K$ . For notational simplicity, we occasionally omit the superscript  $K$  when

no confusion arises. Using its vertices  $\{x_0\}_{i=0}^d$ , we define the edge matrix (of size  $d \times d$ ) of  $K$  (see, e.g., [LH17]) as follows:

$$E = [E_1, \dots, E_d] = [x_1 - x_0, \dots, x_d - x_0].$$

Here, the  $i$ th column vector, given by  $E_i = x_i - x_0$  for  $i = 1, \dots, d$ , represents an edge of the triangle or element  $K$ . Since  $K$  is non-degenerate, the matrix  $E$  is non-singular.

Let us shortly recall about simplices and barycentric coordinates (see, e.g., [Cia91, Sec. 6, p. 66]). Given a family of points  $\{x_i\}_{i=0}^d$  in  $\mathbb{R}^d$  and linearly independent vectors  $\{x_i - x_0\}_{i=0}^d$ , the convex hull of  $\{x_i\}_{i=0}^d$  is called a *simplex* with vertices  $\{x_i\}_{i=0}^d$ . For  $0 \leq i \leq d$ , define  $F_i$  to be the *face* of a simplex  $K$  opposite to  $x_i$ , and define  $n_i$  to be the outward normal to  $F_i$ . In two-spatial dimension, a face is also called an edge.

For a simplex  $K$  in  $\mathbb{R}^d$ , it is often convenient to consider the associated *barycentric coordinates*  $\{\lambda_1, \dots, \lambda_d\}$  defined as follows (cf. [EG04, Eq. (1.37), p. 21]): for  $0 \leq i \leq d$ ,

$$\lambda_i : \mathbb{R}^d \ni x \mapsto \lambda_i(x) = 1 - \frac{(x - x_i) \cdot n_i}{(x_j - x_i) \cdot n_i} = \frac{(x_j - x) \cdot n_i}{(x_j - x_i) \cdot n_i} \in \mathbb{R}, \quad (33)$$

where  $x_j$  is an *arbitrary* vertex in  $F_i$  (this means that  $\lambda_i$  is independent of the choice of the vertex in  $F_i$ ). It is easy to see that  $0 \leq \lambda_i \leq 1$  and  $\lambda_i(x_j) = \delta_{ij}$  for all  $1 \leq i, j \leq d$ . Moreover, it is worth mentioning that for a 2-simplex  $K$ , these coordinates are unique and can be interpreted as the ratio of the area of the 2-simplex (or triangle) formed by  $x$  and the edge opposite to the vertex  $x_i$  to the area of the original triangle. By definition of linear Lagrange basis functions (or, equivalently, the barycentric coordinates reviewed above), we have  $\sum_{i=0}^d \lambda_i = 1$  (see, e.g., [BS08, Proof of Prop. 3.4.5, p. 83]) and  $\sum_{i=0}^d \lambda_i x_i = x$  (see, e.g., [Cia91, Eq. (6.5), p. 66] or [Cia02, Thm. 2.2.1, p. 49]). Notice here that the barycentric coordinates of a point  $x \in \mathbb{R}^d$  are *affine functions* (in fact, affine invariant [GK07]) of the coordinates  $x_1, \dots, x_d$  of  $x$ , that is, they belong to the space  $P_1$ , see [Cia91, Eq. (6.6), p. 66]. In addition, we see that  $\lambda_i$  vanishes at the facet  $F_i$ . From the previously mentioned identities, we easily deduce the following sequence of equalities

$$\sum_{i=1}^d (x_i - x_0) \lambda_i = \sum_{i=0}^d \lambda_i x_i - \lambda_0 x_0 - \sum_{i=1}^d \lambda_i x_0 = \sum_{i=0}^d \lambda_i x_i - x_0 \sum_{i=0}^d \lambda_i = x - x_0.$$

Differentiating both sides of the previous equation with respect to  $x$ , we obtain  $\sum_{i=0}^d (x_i - x_0) (\nabla \lambda_i)^\top = I$ , where  $I$  is the  $d \times d$  identity matrix, or equivalently, in matrix form:

$$E[\nabla \lambda_1, \dots, \nabla \lambda_d]^\top = I.$$

The above equation clearly implies that

$$E^{-\top} = [\nabla \lambda_1, \dots, \nabla \lambda_d]^\top. \quad (34)$$

The edge matrix  $E_K$  associated with  $K$  is not unique, as it depends on the ordering of the vertices. Nevertheless, many geometric properties of  $K$  that do not depend on vertex ordering can still be computed using  $E_K$ . For example, the formula for  $|K|$ —representing the area in two dimensions or the volume in three dimensions—is given by  $\frac{1}{d!} |\det(E_K)|$ . Additionally, the  $i$ th height of  $K$  is given by  $1/|\nabla \lambda_i^K|$ . This leads to the following lemma (see Appendix C for a proof).

**Lemma 6.1.** *Let  $K$  be a non-degenerate triangle with barycentric coordinates  $\{\lambda_1, \lambda_2, \lambda_3\}$ . Then, for each  $i = 1, 2, 3$ , the  $i$ th height of  $K$ , measured from the  $i$ th vertex to the opposite edge, is exactly  $1/|\nabla \lambda_i|$ .*

It follows immediately, by our definition, that

$$\mathbf{a}_K = \min_i \frac{1}{|\nabla \lambda_i^K|}. \quad (35)$$

This quantity will be very useful for estimating matrix norms involving  $E_K$ .

We consider the FE space associated with  $\mathcal{T}_h$  as

$$V_h(\Omega) = \{v \in V(\Omega) \cap C(\bar{\Omega}) \mid v|_K \in P_k(K), \forall K \in \mathcal{T}_h\},$$

where  $V(\Omega)$  is given by (4) and  $P_k(K)$ ,  $k \in \mathbb{N} \cup \{0\}$ , is the set of polynomials of degree no more than  $k$  defined on  $K$ . Any function  $v_h$  in  $V_h(\Omega)$  can be expressed as

$$v_h = \sum_i v_i \psi_i(x),$$

where  $\{\psi_1, \psi_2, \dots\}$  is a basis for  $V_h(\Omega)$ . We distinguish FE basis functions  $\{\psi_1, \psi_2, \dots\}$  from the linear Lagrange basis functions  $\{\phi_i, i = 1, 2, \dots\}$  (with  $\phi_i$  being associated with  $x_i$ ) and emphasize that they can be different (even when  $k = 1$ ).

The FE solution of the BVP (4.4) is obtained by solving the following problem:

**Problem 6.2.** Find  $u_h \in V_h(\Omega)$  such that

$$a(u_h, \psi) = l(\psi), \quad \forall \psi \in V_h(\Omega), \quad (36)$$

where

$$\begin{aligned} a(u_h, \psi) &:= \int_{\Omega} (\sigma \nabla u_h \cdot \nabla \bar{\psi} + k u_h \bar{\psi}) dx + \int_{\Gamma_u} (\alpha + i) u_h \bar{\psi} ds, \\ l(\psi) &:= \int_{\Omega} Q \bar{\psi} dx + \alpha \int_{\Gamma_u} T_a \bar{\psi} ds + i \int_{\Gamma_u} h \bar{\psi} ds, \end{aligned} \quad (37)$$

The following error estimate can be proven similarly to the case of general real-valued elliptic PDEs found in most FEM textbooks (e.g., see [BS08, eq. (6.1.6), p. 156]).

**Proposition 6.3.** Assume that  $u \in H^2(\Omega)$  and the mesh  $\mathcal{T}_h$  is regular. Then,

$$\|\nabla(u_h - u)\|_{L^2(\Omega)} \leq ch \|\Delta u\|_{L^2(\Omega)}, \quad (38)$$

where  $h = \max_{K \in \mathcal{T}_h} h_K$  and  $c > 0$  is a constant independent of  $u$ ,  $u_h$ , and  $\mathcal{T}_h$ .

Assumption 2.1 is sufficient to achieve  $H^2$  regularity for state  $u$ .

The error estimate (38) confirms the stable dependence of the FE solution on the mesh. It ensures that the FE solution remains close to the exact solution for all regular meshes with a maximum element diameter  $h$ , regardless of their variations. However, the estimate does not indicate whether or how the FE solution continuously depends on the mesh. This is what we aim to explain in this work in the spirit of [HH21].

## 7. MESH SENSITIVITY ANALYSIS

To carry out the main task of examining variations in mesh qualities and functions resulting from mesh deformation, we use an approach similar to gradient methods for optimal control (see, e.g., [BH75]) and sensitivity analysis in shape optimization (e.g., see [DZ11, HM03, SZ92]). In this approach, a small deformation in the mesh is introduced, and a finite element formulation is derived. Using this formulation, bounds for the variation in the FE solution resulting from mesh deformation can be established. To achieve this, several lemmas (which are already available in the literature, see [Cia02, EG04, HH21]) are required, and we provide them here, with proofs provided in Appendix C for the convenience of the reader. The mesh sensitivity of the finite element solution is presented in the next section.

We assume that a smooth vector field  $\dot{X} = \dot{X}(x)$  is given on  $\Omega$  and satisfies

$$\|\dot{X}\|_{W^{1,\infty}(\Omega)^d} < \infty. \quad (39)$$

Hereinafter, we say that a vector field is smooth if it satisfies the conditions stated above.

**Remark 7.1.** In shape optimization, the vector field  $\dot{X}$  corresponds to the flow speed generated by the computed shape gradient, such as in (21). More precisely, we can associate the vector field  $\dot{X}$  with the derivative of the perturbation of the identity operator  $T_t$  with respect to the fictitious time parameter  $t$ , i.e.,

$$\frac{d}{dt} T_t \Big|_{t=0} = \theta = \dot{X},$$



provided that  $\theta$  inherits sufficient regularity from the state and adjoint state variables. To obtain a sufficiently regular deformation field  $\theta$  associated with the shape gradient  $dJ(\Omega_0)$ , one approach is to compute its Riesz representative, for instance, in the  $H^3(\Omega)$  Sobolev space. This can be achieved using the well-known Sobolev gradient method [Neu97, DMNV07] (see also [Aze20]). In the numerical solution of Problem 4.6, however, the  $H^1$  Riesz representative of  $dJ(\Omega_0)$  (cf. (70)) is sufficient, as demonstrated in the latter part of Section 9.

We analyze the deformation of the mesh  $\mathcal{T}_h$  while preserving its connectivity, with its vertices moving according to

$$x_i(t) = x_i(0) + t\dot{x}_i, \quad 0 \leq t < t_1, \quad i = 1, 2, \dots, \quad (40)$$

where  $t_1$  is a small positive constant, and the *constant-in-time* nodal velocities are given by  $\dot{x}_i = \dot{X}(x_i(0))$ . We denote the time-dependent mesh as  $\mathcal{T}_h(t)$ . In our numerical approach, we fix the boundary vertices, that is,  $\dot{X} = 0$  on  $\partial\Omega$ . Nevertheless, the analysis extends naturally to cases where boundary points are allowed to move. Moreover, we note that the linearization of any smooth mesh deformation can be expressed in the form of (40). Thus, (40) is sufficiently general.

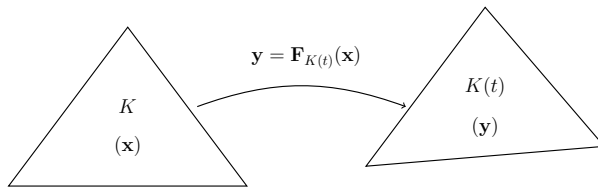


FIGURE 2. Affine mapping  $F_{K(t)}$  from  $K(0) = K \in \mathcal{T}_h$  to  $K(t) \in \mathcal{T}_h(t)$

To analyze the effects of mesh deformation on mesh quantities and functions, we consider the affine mapping  $F_{K(t)}$  that maps  $K(0) = K \in \mathcal{T}_h$  to  $K(t) \in \mathcal{T}_h(t)$ , as shown in Figure 2 (cf. [Cia02, p. 83]), which we assume to be bijective. To avoid notational confusion, we use coordinates  $x$  and  $y$  for  $K(0)$  and  $K(t)$ , respectively. Additionally, we denote quantities and functions in  $y$  by placing a tilde symbol “ $\sim$ ” on top of the corresponding quantities or operators. For instance,  $\nabla := \nabla_x$  represents the gradient operator with respect to  $x$ , while the gradient operator with respect to  $y$  is written as  $\tilde{\nabla} := \nabla_y$ . We examine the effects of mesh deformation by first transforming functions and mesh quantities from  $y$  to  $x$ , and then differentiating them with respect to  $t$ , while keeping  $x$  fixed. The time differentiation is analogous to material differentiation in fluid dynamics. We denote the corresponding derivatives using the dot symbol “ $\dot{\cdot}$ ”.

We begin by considering the time derivatives of the Jacobian matrix and its determinant. Let the Jacobian matrix of  $F_{K(t)}$ , also known as the *deformation gradient*, be denoted by  $J_F = \partial F_{K(t)}(x)/\partial x$ , and let the Jacobian determinant be denoted by  $\mathbb{J} = \det(J_F)$  such that  $\mathbb{J} > 0$ . Consequently, we have the invertibility of  $J_F$  and the bijectivity of  $F_{K(t)}$ . We can express  $J_F$  in terms of the edge matrices of  $K(0)$  and  $K(t)$ . As  $y = F_{K(t)}(x)$  is affine, it can be written as (cf. [EG04, Eq. (1.91), p. 58])

$$y = F_{K(t)}(x) = x_0^K(t) + J_F(x - x_0^K(0)), \quad \forall x \in K(0). \quad (41)$$

Accordingly, we have

$$J_F^{ij} = DF_{K(t)}(x)_{ij} = \frac{\partial y_i}{\partial x_j}, \quad (J_F^{ij})^{-1} = DF_{K(t)}^{-1}(y)_{ij} = \frac{\partial x_i}{\partial y_j}, \quad i, j = 1, \dots, d, \quad (42)$$

where  $x = (x_1, \dots, x_d)$  and  $y = (y_1, \dots, y_d)$ . Now, by taking  $x = x_i^K(0)$  and  $y = x_i^K(t)$ , for  $i = 1, \dots, d$ , sequentially, we get

$$[x_1^K(t) - x_0^K(t), \dots, x_d^K(t) - x_0^K(t)] = J_F[x_1^K(0) - x_0^K(0), \dots, x_d^K(0) - x_0^K(0)],$$

which gives (cf. [HK18, Eq. (3.2)])

$$J_F = E_{K(t)}E_{K(0)}^{-1} \quad \text{and} \quad J_F^{-1} = E_{K(0)}E_{K(t)}^{-1}. \quad (43)$$

For clarity, we remind that  $E_{K(0)}$  and  $E_{K(t)}$  are the edges of the initial and current triangle  $K(0)$  and  $K(t)$ , respectively. From (43), it is evident that  $J_F|_{t=0} = I$ , where  $I$  stands for the  $d \times d$  identity matrix. Differentiating (41) with respect to  $t$  gives

$$\dot{F}_{K(t)}(x) = \dot{x}_0^K(t) + \dot{J}_F(x - x_0^K(0)) = \dot{x}_0^K(t) + \dot{E}_{K(t)}E_{K(0)}^{-1}(x - x_0^K(0)), \quad (44)$$

where, of course,  $\dot{E}_{K(t)} = [\dot{x}_1^K(t) - \dot{x}_0^K(t), \dots, \dot{x}_d^K(t) - \dot{x}_0^K(t)]$ .

Let us also note that the map  $F_{K(t)}(x)$  can be expressed in terms of linear basis functions, that is,

$$F_{K(t)}(x) = \sum_{i=0}^d x_i^K(t) \lambda_i^K(x).$$

Differentiating this with respect to  $t$  gives us

$$\dot{F}_{K(t)}(x) = \sum_{i=0}^d \dot{x}_i^K(t) \lambda_i^K(x). \quad (45)$$

Next, we present some key lemmas to establish the main results of the next section (see Theorem 7.7 and estimate (65)). Their proofs can be found, for instance, in [Cia02, EG04, HH21].

**Lemma 7.2.** *Let  $\dot{X}_h$  be defined as a piecewise linear velocity field, i.e.,*

$$\dot{X}_h = \sum_{i=0}^d \dot{x}_i \lambda_i(x), \quad (46)$$

and assume that the mesh velocity field is smooth. We have the following identities

$$\dot{F}_{K(t)} = \dot{X}_h|_K, \quad \nabla \cdot (\dot{F}_{K(t)}) = \text{tr}(\dot{J}_F) = \text{tr}(\dot{E}_{K(t)}E_{K(0)}^{-1}) = \nabla \cdot (\dot{X}_h|_K), \quad (47)$$

$$\dot{J}_F|_{t=0} = \dot{E}_{K(0)}E_{K(0)}^{-1}, \quad (\dot{J}_F^{-1})|_{t=0} = -\dot{E}_{K(0)}E_{K(0)}^{-1}, \quad \dot{J}|_{t=0} = \nabla \cdot (\dot{X}_h|_K). \quad (48)$$

In addition, the following inequalities hold

$$\|\dot{X}_h\|_{L^\infty(\Omega)^d} \leq \|\dot{X}\|_{L^\infty(\Omega)^d}, \quad \|\nabla \cdot \dot{X}_h\|_{L^\infty(\Omega)^{d \times d}} \leq d \|\nabla \dot{X}\|_{L^\infty(\Omega)^{d \times d}} \max_K \frac{h_K}{a_K}. \quad (49)$$

Let  $\|\cdot\|_2$  and  $\|\cdot\|_F$  denote the usual 2-norm and Frobenius norm (or Hilbert-Schmidt norm) for matrices. Then, it can be shown that the aforementioned norms satisfy the inequality

$$\|M\|_2 \leq \|M\|_F. \quad (50)$$

This inequality is sharp since the equality holds for vectors. Accordingly, we have the next lemma.

**Lemma 7.3.** *For smooth mesh velocity field, there hold the estimates*

$$\|E_{K(0)}^{-1}\|_2 \leq \frac{\sqrt{d}}{a_K} \quad \text{and} \quad \|\dot{E}_{K(0)}\|_2 \leq \sqrt{d} h_K \|\nabla \dot{X}\|_{L^\infty(\Omega)^{d \times d}}. \quad (51)$$

**Remark 7.4.** *In Lemma 7.2 and Lemma 7.3, we assumed that the mesh velocity is smooth which allows one to utilize the identity*

$$\dot{x}_i^K - \dot{x}_0^K = \dot{X}(x_i^K) - \dot{X}(x_0^K) = \int_0^1 \nabla \dot{X}(x_0^K + t(x_i^K - x_0^K)) \cdot (x_i^K - x_0^K) dt,$$

and get the estimates (49)<sub>2</sub> and (51)<sub>2</sub>. If the mesh velocity field is not smooth, then we have

$$|\nabla \cdot \dot{X}_h| \leq \frac{1}{\min_K a_K} \left| \sum_{i=0}^d \dot{x}_i \right|^{\Delta\text{-ineq.}} \leq \frac{1}{\min_K a_K} \sum_{i=0}^d |\dot{X}(x_i(0))|. \quad (52)$$

In the first inequality above, the following identity was used:

$$\nabla \cdot \dot{X}_h = \sum_{i=0}^d \dot{x}_i^K \cdot \nabla \lambda_i^K(x) = \sum_{i=1}^d (\dot{x}_i^K - \dot{x}_0^K) \cdot \nabla \lambda_i^K(x).$$

Taking the supremum of the left- and right-most sides of inequality (52) gives us

$$\|\nabla \cdot \dot{X}_h\|_{L^\infty(\Omega)} \leq \frac{d+1}{\min_K a_K} \|\dot{X}\|_{L^\infty(\Omega)^d}.$$

Similarly, we have  $\|\dot{E}_{K(0)}^{-1}\|_2^2 \leq \sum_{i=1}^d |\dot{x}_i - \dot{x}_0|^2 \leq 2d \|\dot{X}\|_{L^\infty(\Omega)^d}^2$ , from which we get

$$\|\dot{E}_{K(0)}^{-1}\|_2 \leq \sqrt{2d} \|\dot{X}\|_{L^\infty(\Omega)^d}$$

when the mesh velocity field is not smooth.

We next review about the (pseudo) time derivative of functions on  $K$  and  $K(t)$ . First, we mention that in finite element computation, a basis function  $\tilde{\psi}$  on the deformed simplex  $K(t)$  is usually defined as the composition of a basis function  $\psi$  on the reference triangle  $K(0)$  with the affine mapping  $F_{K(t)}$ . That is, we have

$$\tilde{\psi}(y, t) = \psi(F_{K(t)}^{-1}(y)) \quad \stackrel{(41)}{\iff} \quad \tilde{\psi}(F_{K(t)}(x), t) = \psi(x). \quad (53)$$

Taking the derivative of (53) with respect to  $x$  of both sides of the latter equation gives us

$$\tilde{\nabla} \tilde{\psi}(F_{K(t)}(x), t) = J_F^{-\top} \nabla \psi(x), \quad \text{where } J_F^{-\top} = (J_F^{-1})^\top. \quad (54)$$

Component-wise, we have

$$\frac{\partial \tilde{v}(y)}{\partial y_i} = \sum_{j=1}^d \frac{\partial v}{\partial x_j}(x) \frac{\partial x_j}{\partial y_i} \quad \text{and} \quad \frac{\partial v(x)}{\partial x_i} = \sum_{j=1}^d \frac{\partial \tilde{v}}{\partial y_j}(y) \frac{\partial y_j}{\partial x_i}, \quad (55)$$

where the index  $i$  denotes the  $i$ th row of a matrix. Moreover, by differentiating the latter equation in (53) and both sides of equation (54) with respect to  $t$ , and then evaluating at  $t = 0$ , we get

$$\dot{\tilde{\psi}}(\cdot, 0) = 0 \quad \text{and} \quad (\tilde{\nabla} \dot{\tilde{\psi}})(\cdot, 0) = -E_{K(0)}^{-\top} \dot{E}_{K(0)}^\top \nabla \psi, \quad (56)$$

respectively, where we applied (48)<sub>2</sub> in the latter equation.

Let us also consider a function  $f = f(x)$  defined on  $K$  and let  $\tilde{f} = \tilde{f}(y, t) = f(F_{K(t)}(x))$ . Computing the time derivative of  $\tilde{f}$  and then evaluating at  $t = 0$ , we get  $\dot{\tilde{f}}|_{t=0} = \nabla f(F_{K(t)}(x)) \cdot \dot{F}_{K(t)}(x)|_{t=0}$ , and by applying identity (47)<sub>1</sub>, we obtain

$$\dot{\tilde{f}}(\cdot, 0) = \nabla f \cdot \dot{X}_h|_K. \quad (57)$$

In the next lemma, we compute the time derivative at zero of the transport of a finite element approximation function and its corresponding gradient.

**Lemma 7.5.** *Consider a finite element approximation  $v_h = \sum_{i=1}^d v_i \psi_i(x)$ , where  $\{\psi_1, \dots, \psi_d\}$  is a basis for  $V_h(\Omega)$ , and its corresponding transport  $\tilde{v}_h(y, t) = \sum_{i=1}^d v_i(t) \tilde{\psi}(y, t)$ , where  $\{\tilde{\psi}_1, \dots, \tilde{\psi}_d\}$  is a basis for the space  $V_h(\Omega)(t)$ . Then, we have*

$$\begin{aligned} \dot{\tilde{v}}_h(\cdot, 0)|_K &= \dot{v}_h|_K, \\ (\tilde{\nabla} \dot{\tilde{v}}_h)(\cdot, 0)|_K &= -E_K^{-\top} \dot{E}_K^\top \nabla v_h|_K + \nabla \dot{v}_h|_K, \end{aligned} \quad (58)$$

for all  $K \in \mathcal{T}_h$ , where  $\dot{v}_h = \sum_{i=1}^d \dot{v}_i(0) \psi_i(x)$ .

**7.1. Mesh sensitivity analysis for the finite element solution.** In this section we analyze the mesh sensitivity for the FE solution  $u_h = \sum_i u_i \psi_i(x)$  satisfying (36). On the deformed mesh  $\mathcal{T}_h$ , the perturbed FE solution can be expressed as  $\tilde{u} = \sum_i u_i(t) \tilde{\psi}_i(y, t)$ .

Assuming that  $\tilde{u}$  is differentiable, we obtain from Lemma 7.5 that the material derivative of  $\tilde{u}$  at  $t = 0$  is given by

$$\dot{\tilde{u}}_h|_{t=0} = \sum_i \dot{u}_i(0) \psi_i. \quad (59)$$

We denote this by  $\dot{u}_h$ , i.e.,  $\dot{u}_h = \sum_i \dot{u}_i(0) \psi_i$ . This derivative quantifies the change in  $u_h$  due to mesh deformation.

First, we derive the FE formulation for  $\dot{u}_h$  and then establish a bound for  $\|\nabla \dot{u}_h\|_{L^2(\Omega)}$ .

**Theorem 7.6.** *The material derivative  $\dot{u}_h \equiv \sum_i \dot{u}_i(0) \psi_i \in V_h(\Omega)$  uniquely satisfies*

$$\begin{aligned} a(\dot{u}_h, \psi) &= \sum_K \int_K \left( \sigma \nabla u_h \cdot (\dot{E}_K E_K^{-1} + E_K^{-\top} \dot{E}_K^\top) \nabla \bar{\psi} \right) dx \\ &\quad - \sum_{j=0}^1 \int_{\Omega_j} \left[ (\nabla \sigma_j \cdot \dot{X}_h) (\nabla u_h \cdot \nabla \bar{\psi}) + (\nabla k_j \cdot \dot{X}_h) u_h \bar{\psi} - (\nabla Q_j \cdot \dot{X}_h) \bar{\psi} \right] dx \\ &\quad - \sum_{j=0}^1 \int_{\Omega_j} (\sigma_j \nabla u_h \cdot \nabla \bar{\psi} + k_j u_h \bar{\psi} - Q_j \bar{\psi}) (\nabla \cdot \dot{X}_h) dx, \quad \forall \psi \in V_h(\Omega). \end{aligned} \quad (60)$$

*Proof.* The proof proceeds as follows. We start by rewriting the variational formulation of the state's FE solution on the deformed mesh  $\mathcal{T}_h(t)$ . Then, we transform all integrals into the reference mesh and differentiating both sides with respect to time while keeping  $x$  fixed, we obtain the weak formulation of the material derivative. Afterward, we apply Lemma 7.2, equations (56)–(57), and Lemma 7.5, and taking  $t = 0$ , we derive the variational equation 60.

We rewrite (36) into

$$\begin{aligned} &\sum_K \int_K (\sigma \nabla u_h \cdot \nabla \bar{\psi} + k u_h \bar{\psi}) dx + \int_{\Gamma_u} (\alpha + i) u_h \bar{\psi} ds \\ &= \sum_K \int_K (Q \bar{\psi}) dx + \alpha \int_{\Gamma_u} T_a \bar{\psi} ds + i \int_{\Gamma_u} h \bar{\psi} ds, \quad \forall \psi \in V_h(\Omega). \end{aligned} \quad (61)$$

On  $\mathcal{T}_h(t)$ , the perturbed FE solution can be expressed as  $\tilde{u}_h = \sum_i u_i(t) \tilde{\psi}_i(y, t)$ . Then, equation (61) becomes

$$\begin{aligned} &\sum_{K(t)} \int_{K(t)} \left( \sigma \tilde{\nabla} \tilde{u}_h \cdot \tilde{\nabla} \bar{\psi} + k \tilde{u}_h \bar{\psi} \right) dy + \int_{\Gamma_u(t)} (\alpha + i) \tilde{u}_h \bar{\psi} dy \\ &= \sum_{K(t)} \int_{K(t)} \left( Q(y) \bar{\psi} \right) dy + \alpha \int_{\Gamma_u(t)} T_a \bar{\psi} dy + i \int_{\Gamma_u(t)} h \bar{\psi} dy, \quad \forall \bar{\psi} \in V_h(\Omega)(t), \end{aligned}$$

where the test space  $V_h(\Omega)(t) = \text{span}\{\tilde{\psi}_1, \tilde{\psi}_2, \dots\}$ . Note that in above variational equation, we actually have  $\Gamma_u(t) = \Gamma_u(0) \equiv \Gamma_u$  because  $\dot{X} = \dot{X}_h = 0$  on  $\partial\Omega$ .

Transforming all integrals into  $K(0)$ , we obtain

$$\begin{aligned} &\sum_{K(0)} \int_{K(0)} \left( (\sigma \tilde{\nabla} \tilde{u}_h \cdot \tilde{\nabla} \bar{\psi} + k \tilde{u}_h \bar{\psi}) \mathbb{J} \right) dx + \int_{\Gamma_u} (\alpha + i) \tilde{u}_h \bar{\psi} \mathbb{J} |J_F^{-\top} n| ds \\ &= \sum_{K(0)} \int_{K(0)} \left( Q(F_{K(t)}(x)) \bar{\psi} \mathbb{J} \right) dx + \alpha \int_{\Gamma_u} T_a \bar{\psi} \mathbb{J} |J_F^{-\top} n| ds + i \int_{\Gamma_u} h \bar{\psi} \mathbb{J} |J_F^{-\top} n| ds, \quad \forall \bar{\psi} \in V_h(\Omega). \end{aligned}$$

Because  $\mathbb{J} = 1$  and  $|J_F^{-\top} n| = 1$  on  $\Gamma_u$  for all  $t > 0$ , the above equation simplifies to

$$\begin{aligned} & \sum_{K(0)} \int_{K(0)} \left( (\sigma \tilde{\nabla} \tilde{u}_h \cdot \tilde{\nabla} \tilde{\psi} + k \tilde{u}_h \tilde{\psi}) \mathbb{J} \right) dx + \int_{\Gamma_u} (\alpha + i) \tilde{u}_h \tilde{\psi} ds \\ & + \sum_{K(0)} \int_{K(0)} \left( Q(F_{K(t)}(x)) \tilde{\psi} \mathbb{J} \right) dx + \alpha \int_{\Gamma_u} T_a \tilde{\psi} ds + i \int_{\Gamma_u} h \tilde{\psi} ds, \quad \forall \tilde{\psi} \in V_h(\Omega). \end{aligned}$$

Differentiating the above equation with respect to  $t$  while keeping  $x$  fixed, we obtain

$$\begin{aligned} & \sum_{K(0)} \int_{K(0)} \left( (\sigma \dot{\tilde{\nabla}} \tilde{u}_h \cdot \tilde{\nabla} \tilde{\psi} + k \dot{\tilde{u}}_h \tilde{\psi}) \mathbb{J} \right) dx + \int_{\Gamma_u} (\alpha + i) \dot{\tilde{u}}_h \tilde{\psi} ds \\ & = - \sum_{K(0)} \int_{K(0)} \left( (\sigma \tilde{\nabla} \tilde{u}_h \cdot (\dot{\tilde{\nabla}} \tilde{\psi}) + k \tilde{u}_h \dot{\tilde{\psi}}) \mathbb{J} \right) dx - \int_{\Gamma_u} (\alpha + i) \tilde{u}_h \dot{\tilde{\psi}} ds \\ & - \sum_{K(0)} \int_{K(0)} \left( (\dot{\sigma} \tilde{\nabla} \tilde{u}_h \cdot \tilde{\nabla} \tilde{\psi} + \dot{k} \tilde{u}_h \tilde{\psi}) \mathbb{J} \right) dx - \sum_{K(0)} \int_{K(0)} \left( (\sigma \tilde{\nabla} \tilde{u}_h \cdot \tilde{\nabla} \tilde{\psi} + k \tilde{u}_h \tilde{\psi}) \dot{\mathbb{J}} \right) dx \\ & + \sum_{K(0)} \int_{K(0)} \left( \dot{Q} \tilde{\psi} \mathbb{J} \right) dx + \alpha \int_{\Gamma_u} \dot{T}_a \tilde{\psi} ds + i \int_{\Gamma_u} \dot{h} \tilde{\psi} ds \\ & + \sum_{K(0)} \int_{K(0)} \left( Q \dot{\tilde{\psi}} \mathbb{J} \right) dx + \alpha \int_{\Gamma_u} T_a \dot{\tilde{\psi}} ds + i \int_{\Gamma_u} h \dot{\tilde{\psi}} ds \\ & + \sum_{K(0)} \int_{K(0)} \left( Q \tilde{\psi} \dot{\mathbb{J}} \right) dx, \quad \forall \tilde{\psi} \in V_h(\Omega). \end{aligned}$$

Now, applying Lemma 7.2, equations (56)–(57), and Lemma 7.5, while taking  $t = 0$  and noting that  $\mathbb{J} = 1$  and  $y = x$  at  $t = 0$ , we obtain

$$\begin{aligned} & \sum_{K(0)} \int_{K(0)} \left( (\sigma (\nabla \dot{u}_h - E_K^{-\top} \dot{E}_K^{\top} \nabla u_h) \cdot \nabla \bar{\psi} + k \dot{u}_h \bar{\psi}) \right) dx + \int_{\Gamma_u} (\alpha + i) \dot{u}_h \bar{\psi} ds \\ & = - \sum_{K(0)} \int_{K(0)} \left( (\sigma \nabla u_h \cdot (-E_K^{-\top} \dot{E}_K^{\top}) \nabla \bar{\psi}) \right) dx \\ & - \sum_{K(0)} \int_{K(0)} \left( (\nabla \sigma \cdot \dot{X}_h) \nabla u_h \cdot \nabla \bar{\psi} + (\nabla k \cdot \dot{X}_h) u_h \bar{\psi} \right) dx \\ & - \sum_{K(0)} \int_{K(0)} \left( (\sigma \nabla u_h \cdot \nabla \bar{\psi} + k u_h \bar{\psi}) (\nabla \cdot \dot{X}_h) \right) dx \\ & + \sum_{K(0)} \int_{K(0)} \left( (\nabla Q \cdot \dot{X}_h) \bar{\psi} \right) dx + \sum_{K(0)} \int_{K(0)} \left( Q \bar{\psi} (\nabla \cdot \dot{X}_h) \right) dx, \quad \forall \bar{\psi} \in V_h(\Omega). \end{aligned}$$

Since  $K(0) = K$ , the following equation, obtained after some rearrangement, is equivalent to the previous one

$$\begin{aligned} a(\dot{u}_h, \psi) & = \sum_{K(0)} \int_{K(0)} \left( \sigma \nabla u_h \cdot (\dot{E}_K E_K^{-1} + E_K^{-\top} \dot{E}_K^{\top}) \nabla \bar{\psi} \right) dx \\ & - \sum_{K(0)} \int_{K(0)} \left( (\nabla \sigma \cdot \dot{X}_h) \nabla u_h \cdot \nabla \bar{\psi} + (\nabla k \cdot \dot{X}_h) u_h \bar{\psi} - (\nabla Q \cdot \dot{X}_h) \bar{\psi} \right) dx \\ & - \sum_{K(0)} \int_{K(0)} \left( (\sigma \nabla u_h \cdot \nabla \bar{\psi} + k u_h \bar{\psi} - Q \bar{\psi}) (\nabla \cdot \dot{X}_h) \right) dx, \quad \forall \bar{\psi} \in V_h(\Omega). \end{aligned}$$

Noting that  $\Omega = \Omega_1 \cup \bar{\Omega}_0$ , we obtain (60) as desired.

In addition, by the regularity assumptions on  $\sigma$ ,  $k$ , and  $Q$ , together with the bounds in (3), it can be easily verified that  $\dot{u}_h$  uniquely solves (60) in  $V_h(\Omega)$ .  $\square$

Using the previously established theorem, we can readily derive a stability estimate for the material derivative of the state, as stated in the following theorem. Its proof requires the following Poincaré inequality over  $V(\Omega)$ : there exists a constant  $c_P > 0$  such that

$$\|u\|_{L^2(\Omega)} \leq c_P \|\nabla u\|_{L^2(\Omega)^d}, \quad \forall u \in V(\Omega). \quad (62)$$

This inequality can be verified by modifying one of the standard proofs of the Poincaré inequality, namely the proof by contradiction (see, e.g., [DL98, Proof of Prop. 2, p. 127]).

**Theorem 7.7.** *Let  $\Omega$  be a polygonal/polyhedral domain in  $\mathbb{R}^d$ ,  $d \in \{2, 3\}$ ,  $\alpha \in \mathbb{R}_+$ ,  $Q \in H^1(\Omega)$ ,  $T_a \in H^{1/2}(\Gamma_u)$ ,  $h \in H^{1/2}(\Gamma_u)$ , and the known parameters be given such that Assumption 2.1 holds. Let  $\dot{X}$  satisfies (39) and assume that  $\mathcal{T}_h$  is a simplicial mesh with the minimum element height  $\min_K a_K > 0$ . Then, the material derivative of the FE solution to the state problem 4.4 due to mesh deformation is bounded by*

$$\begin{aligned} & c_1 \|\nabla \dot{u}_h\|_{L^2(\Omega)^d} \\ & \leq \left( c_2 \|\nabla \sigma\|_{L^\infty(\Omega)^d} + c_2 c_P^2 \|\nabla k\|_{L^\infty(\Omega)^d} + c_P \|\nabla Q\|_{L^2(\Omega)^d} \right) \|\dot{X}\|_{L^\infty(\Omega)^d} \\ & \quad + d \left( c_P \|Q\|_{L^2(\Omega)} + 3c_2 \|\sigma\|_{L^\infty(\Omega)} + c_2 c_P^2 \|k\|_{L^\infty(\Omega)} \right) \|\nabla \dot{X}\|_{L^\infty(\Omega)^d} \max_K \frac{h_K}{a_K}, \end{aligned} \quad (63)$$

where

$$c_2 = c_2(Q, T_a, h) := c_0 \left( \|Q\|_{H^1(\Omega)} + \|T_a\|_{H^{1/2}(\Gamma_u)} + \|h\|_{H^{1/2}(\Gamma_u)} \right). \quad (64)$$

*Proof.* From Theorem 7.6, we know that  $\dot{u}_h \equiv \sum_i \dot{u}_i(0) \psi_i \in V_h(\Omega)$ . Choosing  $\psi = u_h$  in (60) and then taking the real part on both sides, we obtain the following estimates through the Cauchy-Schwarz inequality (applied twice), the Poincaré inequality (62) (also applied twice), inequality (11) with higher regularity of the data  $Q$ ,  $T_a$ , and  $h$ , and the coercivity estimate (12):

$$\begin{aligned} c_1 \|\nabla \dot{u}_h\|_{L^2(\Omega)^d} & \leq c_2 \|\sigma\|_{L^\infty(\Omega)} \left( 2 \max_K \|\dot{E}_K E_K^{-1}\|_2 + \|\nabla \cdot \dot{X}_h\|_{L^\infty(\Omega)} \right) + c_2 \|\nabla \sigma\|_{L^\infty(\Omega)^d} \|\dot{X}_h\|_{L^\infty(\Omega)^d} \\ & \quad + c_2 c_P^2 (\|\nabla k\|_{L^\infty(\Omega)^d} \|\dot{X}_h\|_{L^\infty(\Omega)^d} + \|k\|_{L^\infty(\Omega)} \|\nabla \cdot \dot{X}_h\|_{L^\infty(\Omega)}) \\ & \quad + c_P (\|\nabla Q\|_{L^2(\Omega)^d} \|\dot{X}_h\|_{L^\infty(\Omega)^d} + \|Q\|_{L^2(\Omega)} \|\nabla \cdot \dot{X}_h\|_{L^\infty(\Omega)}) \end{aligned}$$

where  $c_2 > 0$  is given in (64). Employing Lemma 7.2 and Lemma 7.3, and after some rearrangement, we obtain

$$\begin{aligned} c_1 \|\nabla \dot{u}_h\|_{L^2(\Omega)^d} & \leq \left( c_2 \|\nabla \sigma\|_{L^\infty(\Omega)^d} + c_2 c_P^2 \|\nabla k\|_{L^\infty(\Omega)^d} + c_P \|\nabla Q\|_{L^2(\Omega)^d} \right) \|\dot{X}\|_{L^\infty(\Omega)^d} \\ & \quad + \left( c_P \|Q\|_{L^2(\Omega)} + c_2 \|\sigma\|_{L^\infty(\Omega)} + c_2 c_P^2 \|k\|_{L^\infty(\Omega)} \right) \|\nabla \cdot \dot{X}\|_{L^\infty(\Omega)} \\ & \quad + 2c_2 \|\sigma\|_{L^\infty(\Omega)} \max_K \|\dot{E}_K E_K^{-1}\|_2 \\ & \leq \left( c_2 \|\nabla \sigma\|_{L^\infty(\Omega)^d} + c_2 c_P^2 \|\nabla k\|_{L^\infty(\Omega)^d} + c_P \|\nabla Q\|_{L^2(\Omega)^d} \right) \|\dot{X}\|_{L^\infty(\Omega)^d} \\ & \quad + d \left( c_P \|Q\|_{L^2(\Omega)} + 3c_2 \|\sigma\|_{L^\infty(\Omega)} + c_2 c_P^2 \|k\|_{L^\infty(\Omega)} \right) \|\nabla \dot{X}\|_{L^\infty(\Omega)^{d \times d}} \max_K \frac{h_K}{a_K}, \end{aligned}$$

as desired.  $\square$

Some remarks on the estimate (63) is necessary. The bound in (63) is derived without assuming the mesh is regular. The mesh can be any shape—whether isotropic, anisotropic, uniform, or nonuniform—as long as it is simplicial and has a positive minimum element height ( $\min_K a_K > 0$ ).

For meshes with a large aspect ratio, the factor  $\max_K \frac{h_K}{a_K}$  becomes large, which makes the bound more sensitive to  $\|\nabla \dot{X}\|_{L^2(\Omega)^{d \times d}}$ . The bound also shows that both the size and gradient of the mesh velocity field affect the FE solution. The size is not affected by the mesh element shape, but the effect of the gradient depends on the maximum element aspect ratio  $\max_K \frac{h_K}{a_K}$ .

Additionally, (63) is independent of (fictitious) time derivatives. Therefore,  $\dot{X}$  can be interpreted as mesh displacement rather than velocity. In the context of shape optimization, mesh displacement in a sense corresponds to the perturbation of the identity approach, while mesh velocity represents the speed method. The homogeneity with respect to time derivatives depends on whether the deformation field is autonomous or not (see [BR15, DZ11]). The bound further indicates that changes in the FE solution remain small when both  $\dot{X}$  and  $\nabla \dot{X}$  are small, implying a continuous dependence of the FE solution on the mesh.

**Remark 7.8.** *If the mesh velocity field is not smooth, from Remark 7.4, we can replaced (63) as follows:*

$$\begin{aligned} c_1 \|\nabla \dot{u}_h\|_{L^2(\Omega)^d} &\leq \left( c_2 \|\nabla \sigma\|_{L^\infty(\Omega)^d} + c_2 c_P^2 \|\nabla k\|_{L^\infty(\Omega)^d} + c_P \|\nabla Q\|_{L^2(\Omega)^d} \right) \|\dot{X}\|_{L^\infty(\Omega)^d} \\ &\quad + \left( c_P \|Q\|_{L^2(\Omega)} + c_2 \|\sigma\|_{L^\infty(\Omega)} + c_2 c_P^2 \|k\|_{L^\infty(\Omega)} \right) \frac{d+1}{\min_K a_K} \|\dot{X}\|_{L^\infty(\Omega)^d} \quad (65) \\ &\quad + 2c_2 \|\sigma\|_{L^\infty(\Omega)} \frac{d\sqrt{2}}{\min_K a_K} \|\dot{X}\|_{L^\infty(\Omega)^d}. \end{aligned}$$

For a given mesh,  $\min_K a_K > 0$  is a fixed value. Therefore, inequality (65) shows that the FE solution remains continuously dependent on the mesh, even when the mesh velocity field lacks smoothness. Numerical examples are presented in Subsection 9.4 to illustrate the established results.

## 8. DISCRETIZATION OF THE COST FUNCTION

To numerically solve Problem (4.6), a suitable discretization is required. A standard approach involves discretizing the PDE using a finite element space defined on a computational mesh, denoted by  $\Omega_h$ , where the nodal positions represent the discrete unknown domain. A typical choice is to approximate  $V(\Omega)$  by the finite element space of globally continuous, piecewise linear functions, defined as follows:

$$P_h^1 = \{v \in V(\Omega_h) \cap C(\bar{\Omega}_h) \mid v|_K \in P_1(K), \forall K \in \Omega_h\}, \quad (66)$$

defined over an approximation  $\Omega_h = \mathcal{T}_h(\Omega)$  of  $\Omega$ . Consequently, the “discrete version” of Problem 4.6 is given as follows:

**Problem 8.1.** *Let  $\Omega_h$  be an approximation of  $\Omega$  (i.e., it consists of geometrically conforming simplicial elements  $K$ ) and consider the admissible set of sub-domains  $U_h$  defined as follows:*

$$U_h := \left\{ \Omega_{0,h} \Subset \Omega_o \mid \begin{array}{l} d(x, \partial\Omega_h) > d_o, \forall x \in \Omega_{0,h}, \Omega_{1,h} \text{ is connected, and} \\ \Omega_{0,h} \text{ is a Lipschitz polygonal/polyhedral domain} \end{array} \right\},$$

Find  $\Omega_0^* \in U_h$  such that

$$\Omega_{0,h}^* = \operatorname{argmin}_{\Omega_{0,h} \in U_h} J_h(\Omega_{0,h}) := \operatorname{argmin}_{\Omega_{0,h} \in U_h} \frac{1}{2} \int_{\Omega_h} (u_h^i)^2 dx,$$

where  $u_h^i = \mathfrak{S}\{u_h\}$ ,  $u_h$  uniquely solves (36) in  $P_h^1$ .

Above, the minimization is understood to be taken over the nodal points in  $\Omega_h$ .

Notice the distinction between Problem 8.1 and the continuous case, Problem 4.6. A key difference is that the admissible domains now have lower regularity. As a result, the shape derivative of  $J_h$  cannot be expressed in boundary integral form—that is, in accordance with the Hadamard-Zolésio structure theorem [DZ11, Thm 3.6, p. 479]. This occurs because  $\Omega_h \notin C^{1,1}$ , and thus, even if the data have high regularity,  $u_h \notin H^2(\Omega_h)$ . The lack of  $H^2$  regularity generally prevents transforming the domain integral into a boundary integral via integration by parts; see the last paragraph in [DZ11, Chap. 10, sec. 5.6, p. 562]. For further discussion on this topic, we refer the reader to [EHLW20].

Let us derive the discrete version of (21). For this purpose, we introduce the discrete adjoint equation corresponding to (67):

**Problem 8.2.** Find  $p_h \in P_h^1$  such that

$$a_{\text{adj}}(p_h, v_h) = \int_{\Omega_h} u_h^i \overline{v_h} dx, \quad \forall v_h \in P_h^1. \quad (67)$$

In Problem 8.2, the sesquilinear form  $a_{\text{adj}}$  is essentially given by (20), except that the limits of integration are taken over  $\Omega_h$  and  $\Gamma_{u,h}$ .

Now, directly substituting the state  $u$  and adjoint state  $p$  with their finite element counterparts  $u_h$  and  $p_h$  in (21) produces the correct formula for the shape derivative  $dJ_h(\Omega_h)[\theta_h]$  of the discrete objective  $J_h$ , provided that the perturbation field  $\theta_h$  belongs to the admissible space of (discrete) deformation fields

$$P_h^1(\Omega_h)^d = \{\theta_h \in H_0^1(\Omega_h)^d \cap C(\overline{\Omega_h})^d \mid \theta_h|_K \in P_1(K)^d, \forall K \in \Omega_h\}. \quad (68)$$

**Theorem 8.3.** Let  $u_h \in P_h^1$  and  $p_h \in P_h^1$  be the unique solution to Problem 6.2 and Problem 8.2, respectively. Moreover, let  $\theta_h \in P_h^1(\Omega_h)^d$ . Then,

$$\begin{aligned} dJ_h(\Omega_0)[\theta_h] &= \frac{1}{2} \int_{\Omega_h} \operatorname{div} \theta_h u^i{}^2 dx - \int_{\Omega_h} \operatorname{div} \theta_h \sigma \sum_{j=1}^d (\partial_j u_h^i \partial_j p_h^r - \partial_j u_h^r \partial_j p_h^i) dx \\ &\quad + \int_{\Omega_h} \sigma \sum_{m=1}^d \sum_{j=1}^d \partial_j \theta_{h,m} (\partial_j u_h^i \partial_m p_h^r - \partial_j u_h^r \partial_m p_h^i) dx \\ &\quad + \int_{\Omega_h} \sigma \sum_{m=1}^d \sum_{j=1}^d \partial_j \theta_{h,m} (\partial_m u_h^i \partial_j p_h^r - \partial_m u_h^r \partial_j p_h^i) dx \\ &\quad + \int_{\Omega_h} \operatorname{div} \theta_h k (u_h^i p_h^r - u_h^r p_h^i) dx + \int_{\Omega} \operatorname{div} \theta_h Q p_h^i dx. \end{aligned} \quad (69)$$

The proof of this theorem is similar to the continuous case, so we omit it.

**Remark 8.4.** Theorem 5.1 and Theorem 8.3 are equivalent in terms of obtaining the shape derivative. Additionally, Theorem 8.3 remains true when higher-order Lagrangian finite elements on simplices are used instead of  $P_h^1(\Omega_h)^d$ . However, it is important that  $\theta_h$  remains piecewise linear so that piecewise polynomials are transformed into piecewise polynomials of the same order. Note that this restriction implicitly implies the need to regularize  $\theta_h$  once the property of being piecewise linear is lost.

## 9. NUMERICAL ALGORITHM AND EXAMPLES

This section outlines the numerical implementation of our approach and presents simulations to demonstrate the algorithm's performance. We first address the forward problem and the choice of regularization in the inversion procedure.

**9.1. Forward problem.** The computational setup is as follows: In the forward problem, all known parameters, including the exact geometry of the tumor, are specified. In all cases, we define  $\Omega$  as a rectangle of dimensions  $0.09$  (m)  $\times$   $0.03$  (m), and we assume the following thermal physiological parameters based on [APT11, DL04, PM07]:

$$\begin{aligned} \sigma_1 &= 0.5 \text{ (W/m}^\circ\text{C)}, & \sigma_2 &= 0.75 \text{ (W/m}^\circ\text{C)}, & T_b &= 37^\circ\text{C}, \\ k_1 &= 1998.1 \text{ (W/m}^3\text{ }^\circ\text{C)}, & k_2 &= 7992.4 \text{ (W/m}^3\text{ }^\circ\text{C)}, & T_a &= 25^\circ\text{C}, \\ Q_1 &= 4200 \text{ (W/m}^3), & Q_2 &= 42000 \text{ (W/m}^3), & \alpha &= 10 \text{ (W/m}^2\text{ }^\circ\text{C)}. \end{aligned}$$

The single observed measurement  $h$  is generated synthetically by solving the direct problem (2). To prevent *inverse crimes* [CK19, p. 179], the forward problem is solved with a fine mesh and  $P_2$  basis functions, while inversion uses a coarser mesh and  $P_1$  basis functions. Gaussian noise with zero mean and standard deviation  $\gamma \|h\|_\infty$ , where  $\gamma$  is a free parameter, is added to  $h$  to simulate noise.



**9.2. Numerical algorithm.** The main steps of our numerical algorithm follows a standard approximation procedure (see, e.g., [RA18]), the important details of which we provide as follows.

The tumor shape is approximated by using a domain variation technique implemented with the finite element method, similar to shape optimization methods [Aze94, Aze20, DMNV07]. To prevent unwanted oscillations at the unknown interface, we use an  $H^1$  Riesz' representative of the distributed shape gradient, a common approach in shape optimization [Aze94, Aze20], which prevents instability in the approximation process. This also allows us to obtain the velocity of each nodes in the finite element mesh to realized the domain variation.

To compute an  $H^1$  Riesz' representative of the distributed shape gradient, we compute  $\theta \in H_0^1(\Omega)^d$  by solving the following variational equation

$$b(\theta, \varphi) = -dJ(\Omega_0)[\varphi], \quad \forall \varphi \in H_0^1(\Omega)^d, \quad (70)$$

where  $b : H_0^1(\Omega)^d \times H_0^1(\Omega)^d \rightarrow \mathbb{R}$  denotes the following bounded and  $H_0^1(\Omega)$ -coercive bilinear form

$$b(\theta, \varphi) := c_b \int_{\Omega} (\nabla \theta : \nabla \varphi + \theta \cdot \varphi) dx + (1 - c_b) \int_{\partial \Omega_0} \nabla_{\tau} \theta : \nabla_{\tau} \varphi ds, \quad (71)$$

where  $c_b \in (0, 1]$  is a free parameter [DFOP18]. In this work, we fix  $c_b = 0.5$ .

Equation 70 provides a Sobolev gradient [Neu97] representation of  $-dJ(\Omega_0)$ . In (71), the boundary integral enforces additional regularity of the deformation field on the boundary interface  $\partial \Omega_0$ ; see, e.g., [DFOP18, DMNV07, RAN25]. For more discussion on discrete gradient flows in shape optimization, we refer readers to [DMNV07].

To compute the  $k$ th boundary interface  $\partial \Omega_0^k$ , we carry out the following procedures:

1. *Initialization:* Fix the maximum number of iterations  $K$ ,  $\rho \in (0, 1)$  (or  $\beta > 1$ ) and choose an initial guess  $\partial \omega^0$ .
2. *Iteration:* For  $k = 0, 1, \dots, K$ , do the following:
  - 2.1 Solve the state's and adjoint's variational equations on the current domain  $\Omega^k$ .
  - 2.2 Choose  $t > 0$ , and compute the deformation vector  $\theta^k$  using (70) in  $\Omega^k$ .
  - 2.3 Update the current domain by setting  $\Omega^{k+1} := \{x + t^k \theta^k(x) \in \mathbb{R}^d \mid x \in \Omega^k\}$ .
3. *Stop Test:* Repeat *Iteration* until convergence.

In Step 2.2,  $t^k$  is computed using a backtracking line search inspired by [RA20, p. 281], with the formula

$$t^k = \frac{sJ(\omega^k)}{\sqrt{b(\theta^k, \theta^k)}}$$

at each iteration step  $k$ , where  $s > 0$  is a scaling factor. While the calculation of the step size can be refined, in our experience, the above simple approach already yields effective results. To prevent inverted triangles in the mesh after the update, the step size  $t^k$  is further reduced. The algorithm also terminates when  $t^k < 10^{-8}$ .

**9.3. Regularization strategy and choice of regularization parameter value.** To deal with noisy measurement in our experiment, we will consider the volume functional  $\text{Vol}(\Omega_0) = \rho \int_{\Omega_0} 1 dx$ , where  $\rho$  is a small positive constant. In this case, selecting the regularization parameter  $\rho$  is crucial in the reconstruction process. This parameter can be determined using the discrepancy principle, which requires accurate knowledge of the noise level. However, reliable noise-level information is often unavailable, and errors in noise estimation can reduce reconstruction accuracy using the discrepancy principle. To address this, we propose a heuristic rule for selecting  $\rho$  that does not rely on noise-level information. This rule is based on the balancing principle [CJK10b], originally developed for parameter identification. We apply this technique for the first time in shape optimization. The idea is simple: fix  $\beta > 1$  and compute  $\rho > 0$  such that

$$(\beta - 1)J(\Omega_0) - \text{Vol}(\Omega_0) := (\beta - 1) \frac{1}{2} \int_{\Omega} (u^i)^2 dx - \rho \int_{\Omega_0} 1 dx = 0. \quad (72)$$

This balances the data-fitting term  $J(\Omega_0)$  with the penalty term  $\text{Vol}(\Omega_0)$ , where  $\beta > 1$  controls the trade-off. It eliminates the need for noise-level knowledge and has been successfully applied to linear and nonlinear inverse problems [CJK10a, CJK10b, Cla12, CJ12, IJT11, Mef21]. In this work, we set  $\beta = 2$ .

The motivation for using the abovementioned regularization strategy is to address the difficulty of recovering small and deep tumors. Incorporating the shape derivative of the weighted volume functional,  $d\text{Vol}(\Omega_0)[\theta] = \rho \int_{\Omega_0} \text{div } \theta \, dx$ , in computing the deformation field helps prevent excessive overshooting of the approximate shape. Its effectiveness is demonstrated in subsections 9.7 and 9.8.

Before we move on to numerical examples, we will provide some remarks on the current algorithm. In numerical shape optimization, *adaptive* FEMs are commonly used for space discretization, aiding in mean curvature computation and local mesh refinement [DMNV07]. Curvature expressions naturally arise in perimeter or surface measure penalization, as their shape derivatives involve mean curvature. To prevent mesh degeneration and excessive stretching, we remesh instead of refining adaptively—every ten steps for 2D problems and every five for 3D.

The bilinear form  $b$  defined by (71) is sufficient for recovering the unknown inclusion (i.e., the tumor shape  $\Omega_0$ ). Alternatively, it can be chosen as the elasticity operator (see, e.g., [Aze94, AW96, DFOP18, EHLW20]). This approach, well known in optimal shape design [Aze94, AW96, Aze20], helps maintain mesh quality after deformation. It is based on the intuition that elastic displacements minimize compression (i.e., local volume changes) [DFOP18].

The variational equation (70) can also be analyzed in a discrete setting. Although important, we omit this analysis—along with the comparison of volume and boundary shape gradients (see Remark 4.1)—to avoid making the study too extensive. For further discussion, we refer interested readers to [DMNV07, EHLW20], which examine discrete gradient flows in shape optimization.

Additionally, [EHLW20] introduced a restricted mesh deformation procedure to prevent mesh deterioration or invalidation caused by interior nodes penetrating neighboring cells. In our algorithm, this issue is handled by reducing the step size. For more details on restricted mesh deformation, we refer readers to [EHLW20].

**9.4. Mesh sensitivity: numerical examples.** Here, we present numerical experiments to support the results established in subsection 7.1. The main observation is that for a smooth velocity field, stability is independent of the mesh, while for a non-smooth velocity field, it becomes mesh-dependent.

The results of the numerical investigation on mesh sensitivity are summarized in Figure 3 and Figure 4 for the 2D and 3D cases, respectively. These figures correspond to the numerical experiments conducted in subsections 9.6–9.8. The figures illustrate the error convergence behavior for exact and noisy measurements. When exact measurements are used, the deformation remains smooth, leading to a convergence rate that is independent of the mesh size. In contrast, under noisy measurements, the deformation becomes non-smooth, and the convergence behavior strongly depends on the mesh resolution. These corroborate the results established in Theorem 7.7 and in equation (65). Additionally, the presence of noise introduces instability, as seen in the increased values in the error plots. This highlights the essential role of measurement accuracy in maintaining robust and consistent numerical convergence. If the measurements are noisy and cannot be improved, we can only resort to using regularization methods to achieve at least a stable approximation. These methods help reduce the impact of noise and provide more reliable numerical results.

We also examine the effect of the free parameter  $c_b$ , which appears in (71), on the stability of the material derivative with respect to mesh deformation. Figure 5 illustrates how different values of this parameter influence error convergence in computing the Riesz representative of the shape gradient in the 2D case. The plots show that with exact measurements, all values of  $c_b$  exhibit similar convergence trends. However, when noise is introduced, larger values of  $c_b$  lead to smoother and more stable error decay, indicating that the computed deformation fields remain more regular across the mesh. In contrast, smaller values of  $c_b$  make the method more sensitive

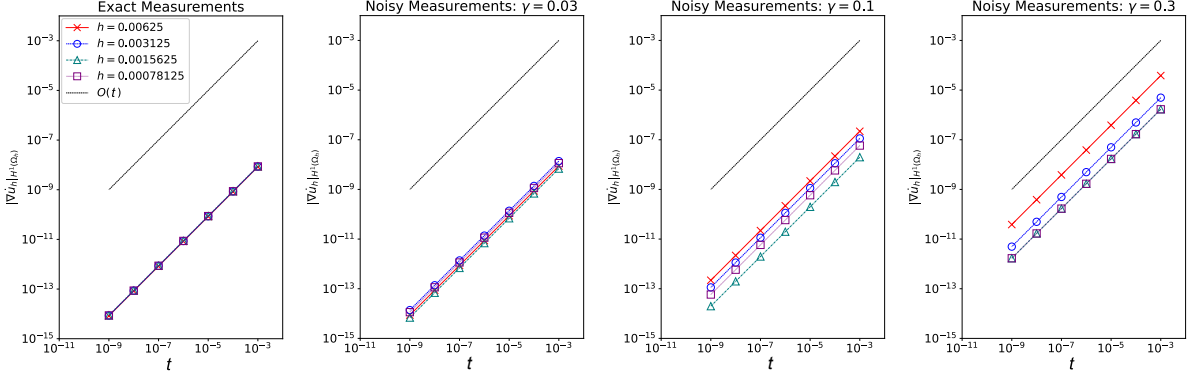


FIGURE 3. Error-of-convergences with exact and noisy measurements for 2D test case

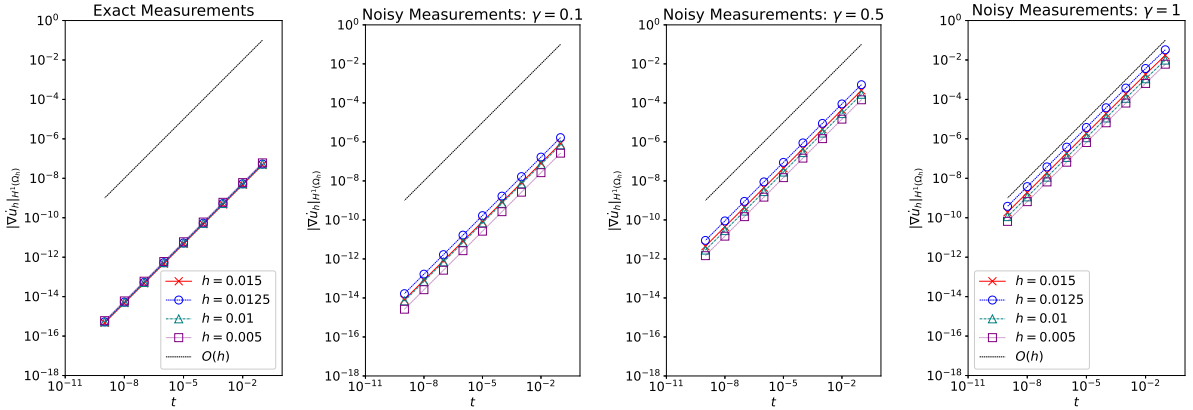


FIGURE 4. Error-of-convergences with exact and noisy measurements for 3D test case

to noise, resulting in erratic error curves and less stable deformations, as expected. While a higher  $c_b$  enhances robustness and prevents excessive local deformations, an excessively large value may over-regularize the deformation, potentially obscuring finer details. Thus, selecting an appropriate  $c_b$  is essential for balancing smoothness and sensitivity, ensuring stability under noise while preserving accuracy in shape gradient representation. In conclusion, for low noise levels ( $< 10\%$ ), the scheme remains generally stable across all tested mesh sizes for  $c_b > 10^{-5}$ . Specifically, step sizes of  $t \leq \varepsilon_1$  ( $< 10^{-3}$ ) result in  $\|\nabla \hat{u}\|_{L^2(\Omega)} < \varepsilon_1$ .

Although not shown, we emphasize that similar convergence behavior is observed in the 3D case. We fix  $c_b = 0.5$  in subsections 9.6–9.8.

**9.5. Preliminary tests.** Before examining specific numerical examples of the inverse problem, we first conduct some preliminary tests on the solution of the forward problem. These tests focus on how the size and location of the tumor affect the skin surface temperature, as well as the impact of noise on the temperature profile. The results will help us establish a good initial guess for the reconstruction.

The numerical results in Figure 6 illustrate the relationship between tumor size and location (lower plots) and the corresponding skin surface temperature profile (upper plots). Tumors closer to the skin or with larger dimensions produce higher and sharper peaks in the temperature profile, while smaller or deeper tumors result in subtler variations. The spatial arrangement of tumors is evident in the temperature distribution, as peaks correspond to their positions. Furthermore, irregular tumor shapes, such as elliptical forms, generate broader or asymmetric temperature patterns. These observations highlight the sensitivity of skin surface temperature to underlying tumor characteristics, a crucial factor for non-invasive diagnostic methods. Notably, the results align with experimental findings reported in the literature. We will use these numerical results to guide the initialization of tumor shapes in the numerical approximation

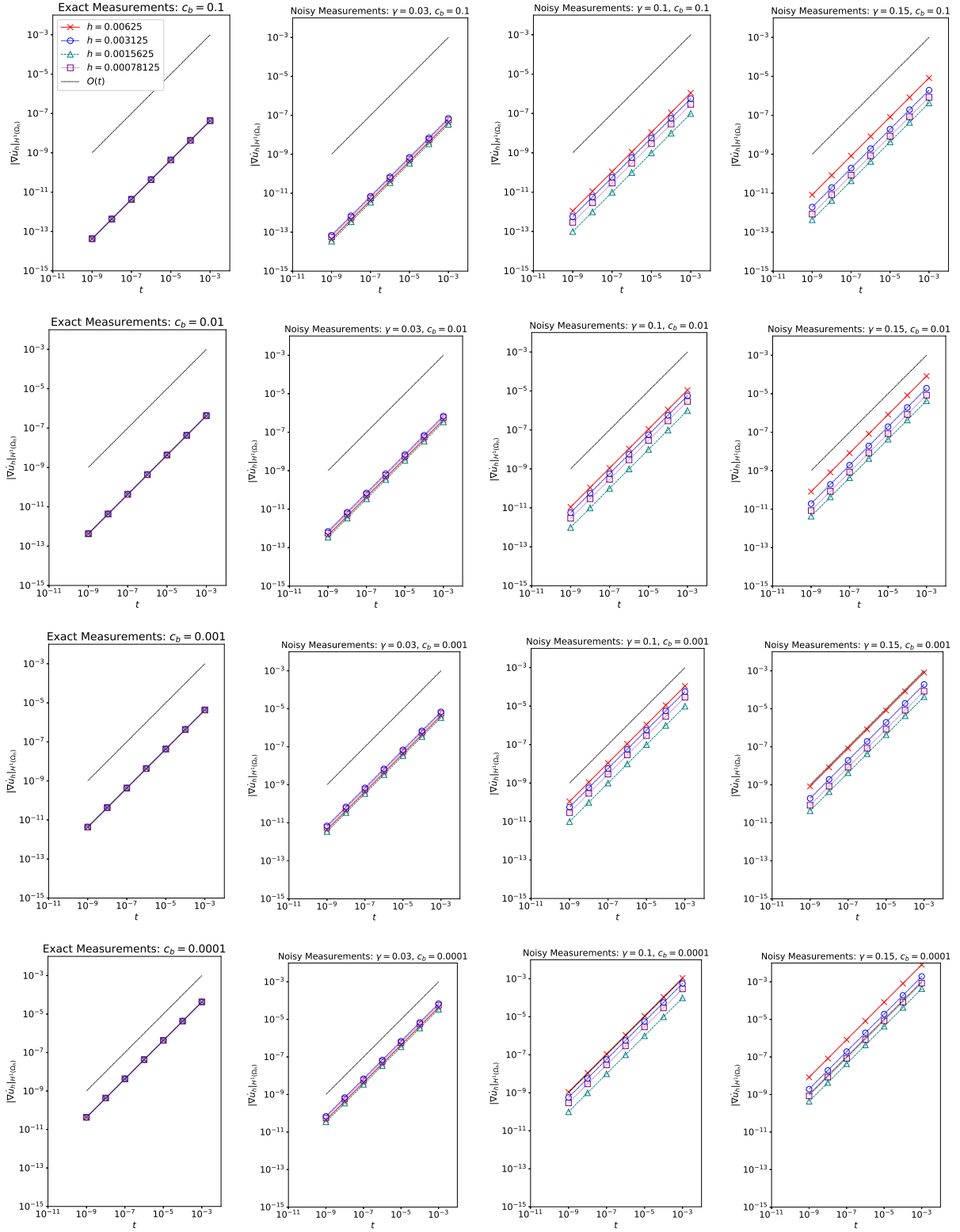


FIGURE 5. Error-of-convergences with exact and noisy measurements for 2D test case testing the effect of  $c_b$ .

for solving the subsequent inverse problems. It is worth noting that a similar idea was used in [RA18], but in the context of cavity detection.

The top row of Figure 7 shows that increasing noise levels ( $\gamma = 0.005, 0.008, 0.01$ ) introduce fluctuations in the skin surface temperature profile, making it less smooth and obscuring finer

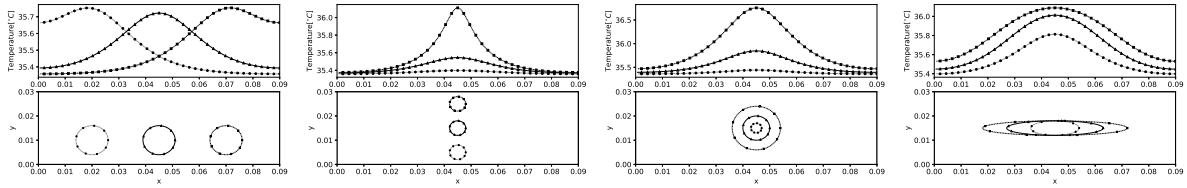


FIGURE 6. The effect of size and location of the tumor on the skin surface temperature profile

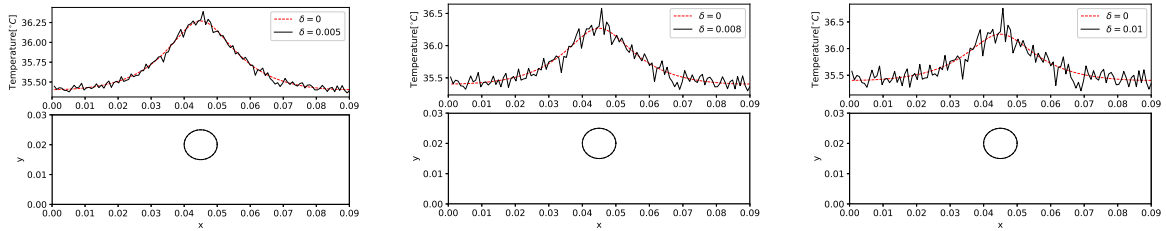


FIGURE 7. The effect of noise level on the skin surface temperature profile

details. However, even in the presence of noise, the location of the tumor (indicated in the bottom row) can still be inferred from the localized temperature rise, though higher noise levels make this more challenging.

It is very important to reiterate at this point that *the present problem is highly ill-posed*, meaning that even small measurement errors can lead to large differences in the identified shape. As a result, an accurate reconstruction of the tumor's geometry cannot be expected, and proper regularization is necessary to mitigate this discrepancy to some extent.

**9.6. Numerical example 1.** We now consider the identification of a circular tumor centered at  $(0.045, 0.020)$  with a radius of  $0.005$  (m). The measured data is assumed to contain  $\gamma = 1\%$  noise. Figure 8 presents the numerical results for tumor shape reconstruction based on temperature measurements on the skin surface.

Panel (a) shows the initial setup, where the temperature profile is fitted with an 11th-order polynomial to identify the peak, which determines the initial guess for the tumor location. The bottom plot depicts the location of the exact tumor (solid line) and the initial guess (dashed line), centered at  $(x_0, y_0) = (0.046, 0.01)$ .

Panel (b) shows cost function histories for different initial radii  $r_0$ . The top plot compares cost values over iterations for  $r_0 = 0.004, 0.005$ , and  $0.006$ , where  $r_0 = 0.005$  yields the lowest final cost, providing the best tumor approximation. Meanwhile, the bottom plot shows gradient norm histories, demonstrating stable convergence. We comment that the method is sensitive to initial condition especially when the initial guess is far from the exact location of the tumor—as expected. We will elaborate more on this subject in the next subsection.

Panel (c) depicts the evolution of the real part of the state solution  $u$  and the free boundary when  $r_0 = 0.005$ . The top plot shows the temporal evolution of the real part of  $u$  (distributions of values on the skin surface  $\Gamma_u$ ), while the bottom plot visualizes the tumor boundary deformation, with colors indicating iteration progress. Evidently, the final boundary closely approximates the true tumor shape.

Panel (d) presents the imaginary part of  $u$  and compares the exact, initial, and final tumor boundaries. The top plot illustrates the histories of the imaginary part of  $u$  (the distribution of values on the skin surface  $\Gamma_u$ ), which is essentially the value evaluated for the reconstruction of the tumor shape. The bottom plot shows a reasonable reconstruction, depicted by dotted red lines, of the exact tumor shape (in solid blue) from the initial guess represented by black dashed lines, thereby validating the reconstruction approach.

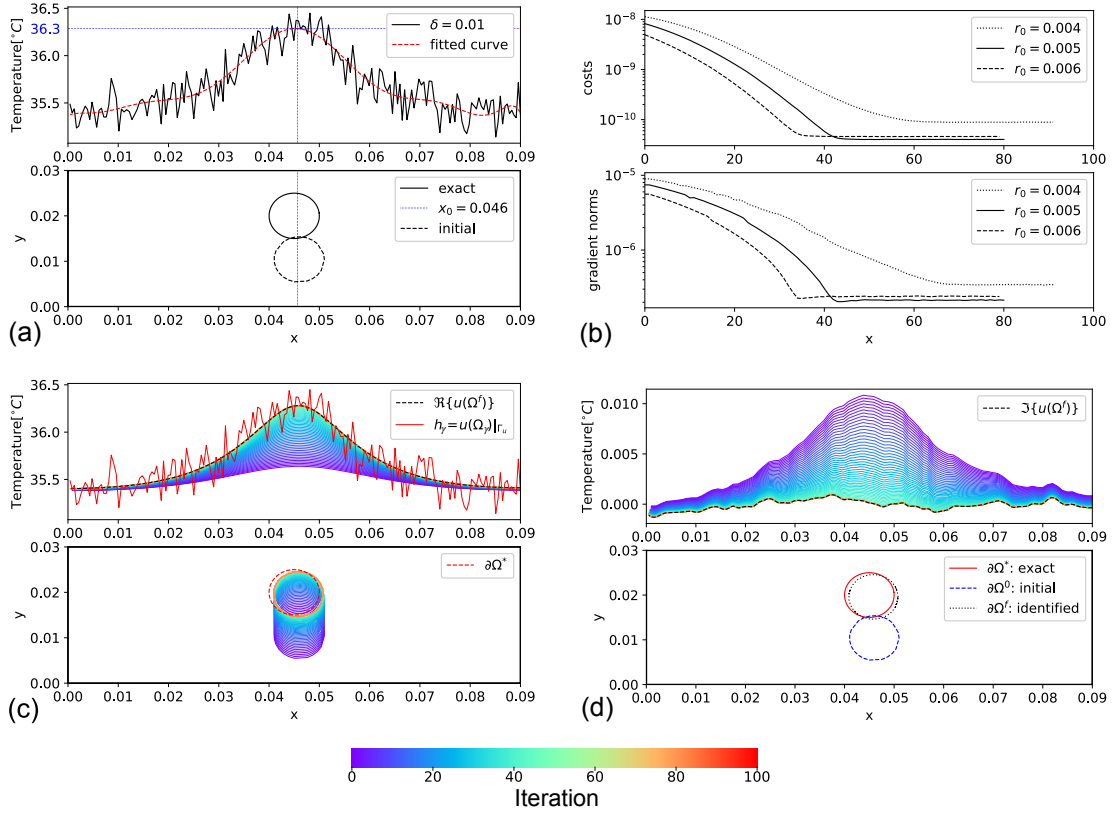


FIGURE 8. (a) Temperature profile on skin surface with noise level  $\gamma = 0.01$  and the initial setup; (b) cost histories for different values of the initial radius  $r_0$ ; (c) evolution of the real part of  $u$  (top) and free boundary transformation (bottom); (d) evolution of the imaginary part of  $u$  (top) and comparison of the exact, initial, and final free boundaries.

**9.7. Numerical example 2.** We next consider identifying a smaller, deeper circular tumor centered at  $(0.045, 0.015)$  with a radius of  $0.003$  (m). With  $\gamma = 1\%$  noise in the measured data, we examine the sensitivity of the method to the initial guess.

Figures 9 and 10 display the numerical results for tumor shape reconstruction using various initial guesses for size and location. The second set of results, shown in Figure 10, omits the peak measured temperature profile on the skin, which is typically used to guide the choice of the initial guess location. These figures underscore the sensitivity of the reconstruction to the initial guess. Notably, a smaller cost value does not always correspond to a more accurate reconstruction for smaller or deeper tumors, regardless of whether the shape is initialized near the exact location based on the peak temperature profile (see Figure 9). However, relying solely on the initial cost value, it is observed that the cases with  $r_0 = 0.003$  or  $0.0025$  consistently yields the lowest cost, while  $r_0 = 0.002$  gives the highest, suggesting that the two former choices provide better approximations of the tumor size. These results aligns with expectations, as the ill-posedness of the inverse problem increases when the target shape is located farther from the measurement region.

Now, to address the aforementioned issue, we apply a penalization using a weighted volume functional combined with the balancing principle, as described in subsection 9.3. This approach helps reduce errors and prevent overshooting in the shape approximation. The effectiveness of our approach is evident from the numerical results in Figure 11, where improved shape approximation and reduced reconstruction errors are observed with  $r_0 = 0.0025$  and  $r_0 = 0.003$ . The figure also shows the histories of values for the cost, gradient norms, and values of the parameter  $\rho$ . Once again, we observed that relying solely on the computed final cost values can be misleading when determining the best approximation among the tested initial guesses. Nevertheless,

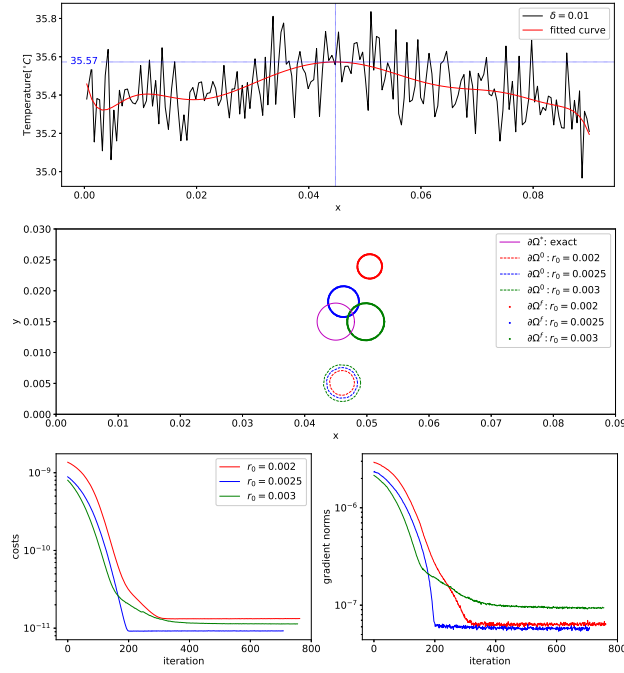


FIGURE 9. (Top) Temperature profile on the skin surface with a noise level of  $\gamma = 0.01$ ; (second row) comparison of the exact, initial, and final free boundaries; (bottom) cost and gradient norm histories for different sizes and locations of the initial guess.

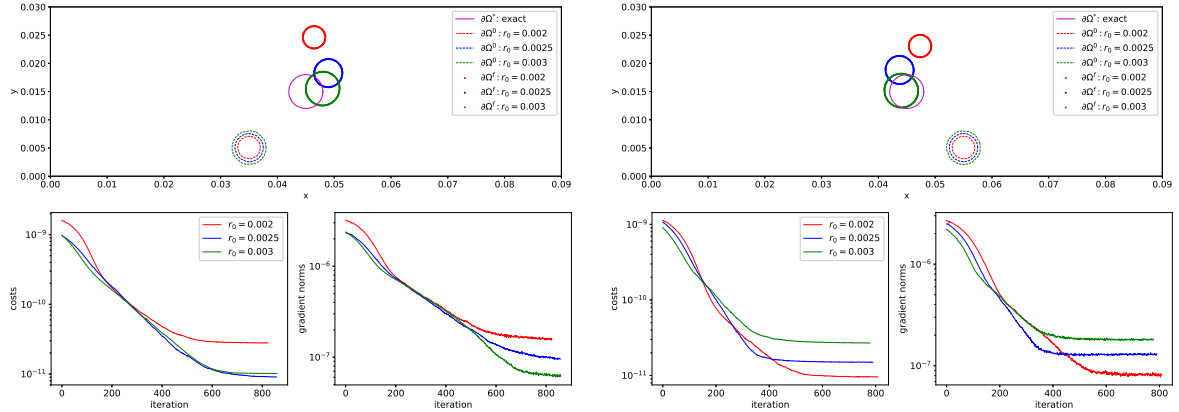


FIGURE 10. (Top) Comparison of the exact, initial, and final free boundaries; (bottom) cost and gradient norm histories for different sizes and locations of the initial guess.

as shown in Figure 12, the reconstruction with  $r_0 = 0.003$  yields the best approximation, as its final temperature profile on the skin most closely matches the fitted curve corresponding to the noisy measured data. In conclusion, utilizing the measured temperature profile on the skin before and after the approximation process enables accurate tumor reconstruction, even in the presence of measurement noise.

**9.8. Numerical example in 3D.** We also test our numerical method in the case of three spatial dimensions. We consider the real shape of the biological tissue of a woman's breast (see Figure 13 for an illustration), which is approximated by half of an ellipsoid with semi-axes of dimensions  $R_1 = 0.07$ ,  $R_2 = 0.06$ , and  $R_3 = 0.07$  (m), while the shape of the tumor is approximated by an ellipsoid with semi-axes of dimensions  $r_1^* = 0.0175$  (m),  $r_2^* = 0.0125$  (m), and  $r_3^* = 0.035$  (m), and center position  $(x_1^*, x_2^*, x_3^*) = (0.015, 0.015, 0.0125)$  (m). The choice of

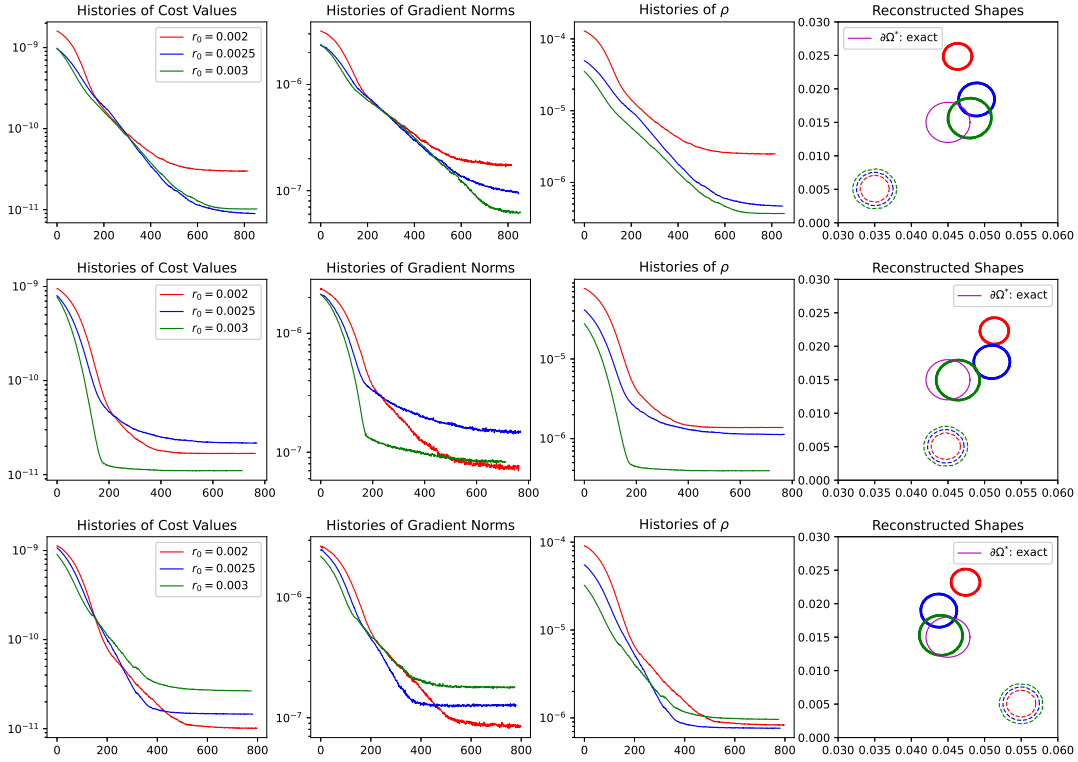


FIGURE 11. Reconstruction results with volume penalization coupled with the balancing principle

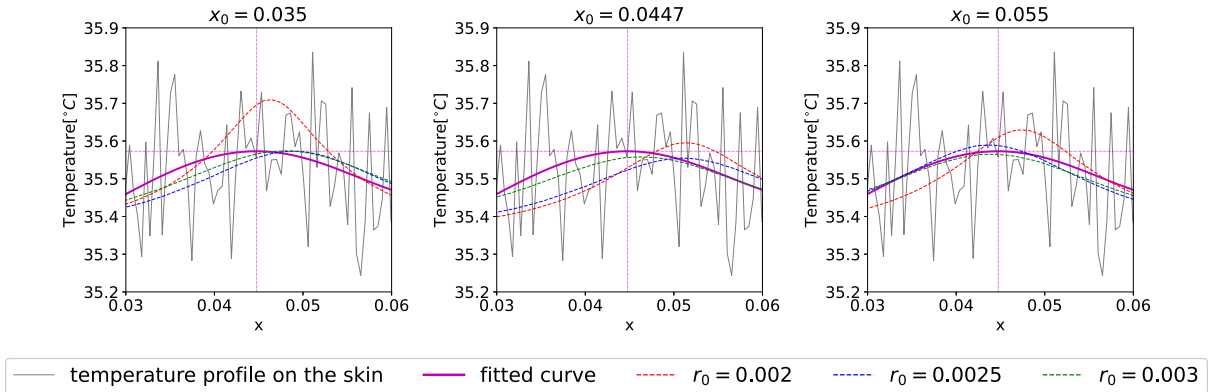


FIGURE 12. Comparison of the measured noisy skin temperature profile, the fitted curve, and the final temperature profiles corresponding to the computed shapes shown in Figure 11.

numerical values for the coefficients is as given in subsection 9.1, and the computational setup is essentially the same as in the 2D case.

Figure 14 shows the tumor’s size, location, and temperature distribution on the skin surface and inside the domain. The plots show an expected increase in skin temperature around the tumor, as expected. Figure 15 shows the temperature distribution with different contour levels. We emphasize that the location of the tumor can be inferred from the plots, but its size is difficult to estimate due to the geometry of the breast.

We now consider the same case with 1% noise. The measured skin temperature is shown in Figure 16. Notice that, despite the presence of noise in the measured temperature, the distribution plot still provides a reliable estimate of the tumor location, at least when viewed on the  $xy$ -plane. Using this information, we initialized our approximation with an elliptical



tumor shape and radii  $(r_1^0, r_2^0, r_3^0) = (\varsigma r_1^*, \varsigma r_2^*, \varsigma r_3^*)$ , where  $\varsigma \in \{0.8, 0.9, 1\}$ , as shown in Figure 17 (in light color). The exact shape is shown in yellow, while the identified shapes are in magenta. The left panel shows results without volume penalization and the balancing principle (72), while the right panel includes this regularization strategy. The purpose of the regularization strategy is to identify the best approximation of the tumor shape from the cost history as we have done in the previous section. Note that the computed temperature profile on the skin (see Figure 18), as opposed to the 2D case (see Figure 12) does not provide enough information to assess the accuracy of the reconstruction, as we cannot tell whether the small or large initial guess leads to a better recovery of the tumor shape. Nevertheless, in all cases, whether or not the regularization strategy is applied, the plots in Figure 19 show that the smallest initial cost value occurs when  $\varsigma = 1$ . The lines labeled  $\partial\Omega_0^{(1)}$ ,  $\partial\Omega_0^{(2)}$ , and  $\partial\Omega_0^{(3)}$  correspond to  $\varsigma = 0.8, 0.9$ , and  $1$ , respectively. Furthermore, in the bottom row, which displays the results with regularization applied, the final cost value is lowest when the shape is initialized with  $\varsigma = 0.9$  or  $\varsigma = 1$ , with  $\varsigma = 1$  yielding the smallest value at the final iteration. Figure 20 shows the mesh profile for the exact and the recovered shape in the case  $\varsigma = 1$ .

As observed in the 2D case, the measured temperature profile on the skin, both before and after the approximation process, enables accurate tumor reconstruction even in the presence of measurement noise. This observation extends to the three-dimensional case, where the strategy for determining the best approximation remains effective.

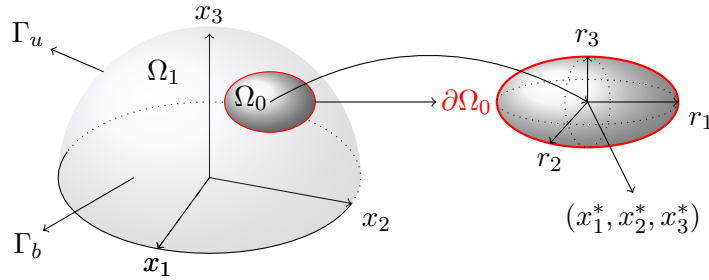


FIGURE 13. Breast tissue with tumor

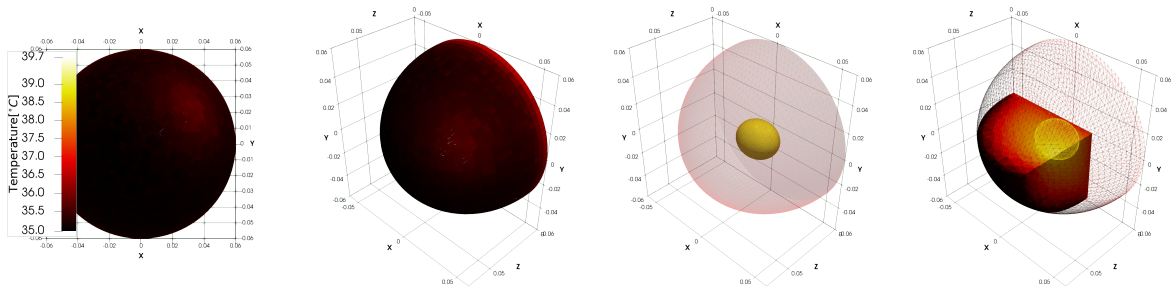


FIGURE 14. Exact location of tumor and temperature distribution

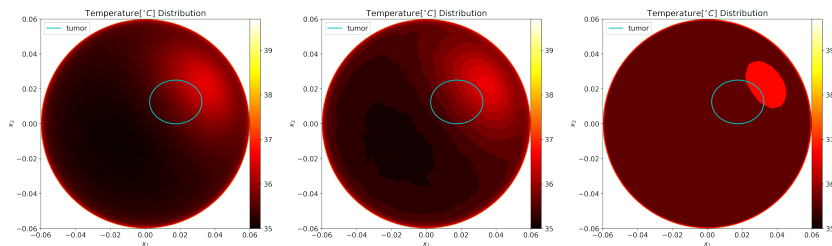


FIGURE 15. Exact temperature distribution plotted with different contour levels

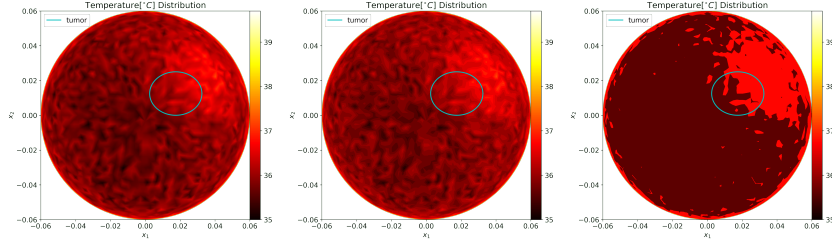


FIGURE 16. Temperature distribution under 1% noise level plotted with different contour levels without the application of volume penalization and the balancing principle (72)

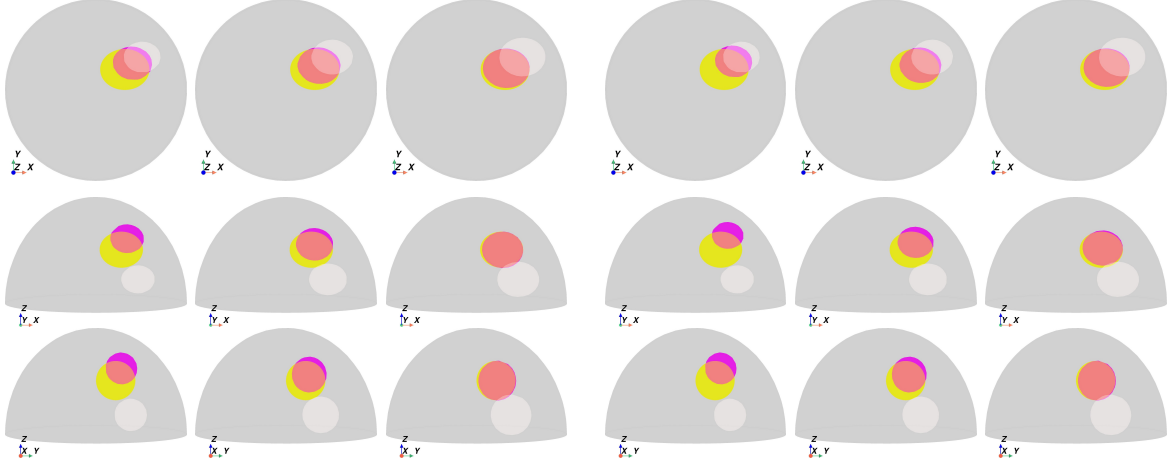


FIGURE 17. Recovered shapes (magenta) from different initial guesses (light color) versus exact tumor (yellow) from various views. Left panel: without volume penalization and balancing principle (72). Right panel: with regularization. On each panel, from left to right, the columns correspond to  $\partial\Omega_0^{(1)}$ ,  $\partial\Omega_0^{(2)}$ , and  $\partial\Omega_0^{(3)}$ .

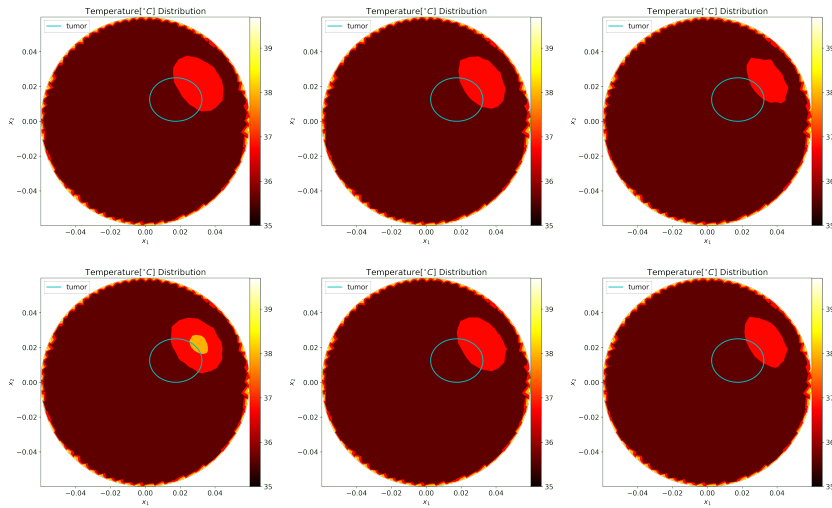


FIGURE 18. Temperature distributions on recovered shapes plotted with three contour levels. The top row shows results without volume penalization and without the balancing principle (72), while the bottom row includes regularization. From left to right, the columns correspond to  $\partial\Omega_0^{(1)}$ ,  $\partial\Omega_0^{(2)}$ , and  $\partial\Omega_0^{(3)}$ .

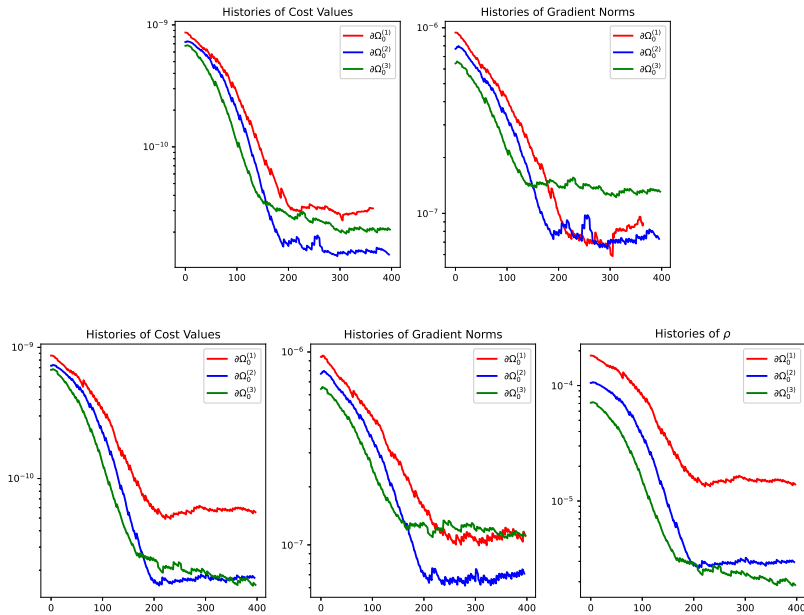


FIGURE 19. Histories of values of the cost and gradient norms. Top row: without volume penalization and balancing principle (72); bottom row: with regularization. The bottom row also shows the histories of values of the parameter  $\rho$  in equation (72).

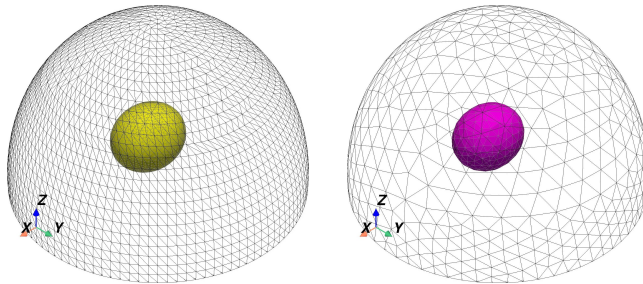


FIGURE 20. The exact (yellow) and computed (magenta) shape corresponding to  $\zeta = 1$ .

## 10. CONCLUSION

This study addressed a tumor localization problem using skin temperature profiles combined with a non-conventional shape optimization approach. The numerical method used is based on the  $H^1$  Riesz representative of the distributed shape gradient, departing from the usual method of using the boundary-type shape gradient. The surface temperature distribution determined the initial estimate of the tumor position. By comparing final cost values for different initial radii, a reasonable tumor approximation is achievable, even with noisy data. Thanks to the weighted penalization of the volume integral coupled with the balancing principle, an improved recovery of the tumor shape is obtained. The proposed Lagrangian-type shape optimization method effectively minimizes the cost function and ensures stable convergence, demonstrating its potential for fair tumor localization.

As a future direction, we aim to extend the Pennes bioheat equation by relaxing its assumptions of constant arterial blood temperature and uniform perfusion, which may not always hold. Ongoing research focuses on incorporating spatially varying perfusion, nonlinear tissue properties, and time-dependent effects to improve the model's accuracy and applicability. Furthermore, the simultaneous recovery of tumor region parameters and geometry using information about skin surface temperature is also an ongoing area of investigation by the author. The results will be reported in a separate venue.

## REFERENCES

- [Afr22] L. Afraites. A new coupled complex boundary method (CCBM) for an inverse obstacle problem. *Discrete Contin. Dyn. Syst. Ser. S*, 15(1):23–40, 2022.
- [AMN22] L. Afraites, C. Masnaoui, and M. Nachaoui. Shape optimization method for an inverse geometric source problem and stability at critical shape. *Discrete Contin. Dyn. Syst. Ser. S*, 15(1):1–21, 2022.
- [APT11] J. P. Agnelli, C. Padra, and C. V. Turner. Shape optimization for tumor location. *Comput. Math. Appl.*, 62:4068–4081, 2011.
- [AR25] L. Afraites and J. F. T. Rabago. Shape optimization methods for detecting an unknown boundary with the Robin condition by a single measurement. *Discrete Contin. Dyn. Syst. Ser. S*, 18(1):43–76, 2025.
- [AW96] H. Azegami and Z. Q. Wu. Domain optimization analysis in linear elastic problems: approach using traction method. *SME Int. J., Ser. A.*, 39:272–278, 1996.
- [Aze94] H. Azegami. A solution to domain optimization problems. *Trans. Jpn. Soc. Mech. Eng., Ser. A.*, 60:1479–1486, 1994.
- [Aze20] H. Azegami. *Shape Optimization Problems*, volume 164 of *Springer Optimization and Its Applications*. Springer, Singapore, 2020.
- [BH75] A. E. Bryson and Y.-C. Ho. *Applied Optimal Control: Optimization, Estimation, and Control*. Taylor & Francis, 1975.
- [BM<sup>+</sup>09] G. A. Santa Cruz 1, J. Bertotti, J. Marín, S. J. González, S. Gossio, D. Alvarez, B. M. C. Roth, P. Menéndez, M. D. Pereira, M. Albero, L. Cubau, P. Orellano, and S. J. Liberman. Dynamic infrared imaging of cutaneous melanoma and normal skin in patients treated with BNCT. *Appl. Radiat. Isot.*, 67:S54–S58, 2009.
- [Bow85] H. F. Bowman. *Estimation of tissue blood flow*, volume I of *Heat Transfer in Medicine and Biology*, pages 193–230. Plenum Press, NY, USA, 1985.
- [BP13] J. B. Bacani and G. H. Peichl. On the first-order shape derivative of the Kohn-Vogelius cost functional of the Bernoulli problem. *Abstr. Appl. Anal.*, 2013:19 pp. Article ID 384320, 2013.
- [BR15] J. B. Bacani and J. F. T. Rabago. On the second-order shape derivative of the Kohn-Vogelius objective functional using the velocity method. *Int. J. Differ. Equ.*, 2015:10 pp. Article ID 954836, 2015.
- [BS08] S. C. Brenner and L. R. Scott. *The Mathematical Theory of Finite Element Methods*. Springer-Verlag, New York, 3rd edition, 2008.
- [CGHZ14] X. L. Cheng, R. F. Gong, W. Han, and X. Zheng. A novel coupled complex boundary method for solving inverse source problems. *Inverse Problems*, page Article 055002, 2014.
- [Cha85] J. C. Chato. *Measurement of thermal properties of biological materials*, volume I of *Heat Transfer in Medicine and Biology*, pages 167–173. Plenum Press, NY, USA, 1985.
- [Cia91] P. G. Ciarlet. *Finite Element Methods*, volume II of *Handbook of Numerical Analysis*, chapter Basic Error Estimates for Elliptic Problems. Elsevier Science Publishers B. V., North-Holland, Amsterdam, 1991.
- [Cia02] P. G. Ciarlet. *The Finite Element Method for Elliptic Problems*. SIAM, Philadelphia, PA, 2nd edition, 2002.
- [CJ12] C. Clason and B. Jin. A semismooth Newton method for nonlinear parameter identification problems with impulsive noise. *SIAM J. Imaging Sci.*, 5:505–536, 2012.
- [CJK10a] C. Clason, B. Jin, and K. Kunisch. A duality-based splitting method for  $L^1$ -tv image restoration with automatic regularization parameter choice. *SIAM J. Sci. Comput.*, 32:1484–1505, 2010.
- [CJK10b] C. Clason, B. Jin, and K. Kunisch. A semismooth newton method for  $L^1$  data fitting with automatic choice of regularization parameters and noise calibration. *SIAM J. Imaging Sci.*, 3:199–231, 2010.
- [CK19] D. Colton and R. Kress. *Inverse Acoustic and Electromagnetic Scattering Theory*. Springer-Verlag, New York, 4th edition, 2019.
- [Cla12] C. Clason.  $L^\infty$  fitting for inverse problems with uniform noise. *Inverse Probl.*, 28:104007, 2012.
- [CS85] R. Correa and A. Seeger. Directional derivative of a mimimax function. *Nonlinear Anal.*, 9:13–22, 1985.
- [DB71] J. W. Draper and J. W. Boag. Skin temperature distributions over veins and tumors. *Phys. Med. Biol.*, 16:645–656, 1971.
- [DFOP18] C. Dapogny, P. Frey, F. Omnès, and Y. Privat. Geometrical shape optimization in fluid mechanics using FreeFEM++. *Struct. Multidiscip. Optim.*, 58:2761–2788, 2018.
- [DL98] R. Dautray and J.-L. Lions. *Mathematical Analysis and Numerical Methods for Science and Technology*, volume 2. Springer, 1998.
- [DL04] Z. Deng and J. Liu. Mathematical modeling of temperature over skin surface and its implementation in thermal disease diagnostics. *Comput. Biol. Med.*, 34:495–521, 2004.
- [DMNV07] G. Doğan, P. Morin, R.H. Nochetto, and M. Verani. Discrete gradient flows for shape optimization and applications. *Comput. Methods Appl. Mech. Engrg.*, 196:3898–3914, 2007.
- [DZ88] M. C. Delfour and J.-P. Zolésio. Shape sensitivity analysis by min-max differentiability. *SIAM J. Control Optim.*, 26(4):834–862, 1988.

- [DZ11] M. C. Delfour and J.-P. Zolésio. *Shapes and Geometries: Metrics, Analysis, Differential Calculus, and Optimization*, volume 22 of *Adv. Des. Control*. SIAM, Philadelphia, 2nd edition, 2011.
- [EG04] A. Ern and J.-L. Guermond. *Theory and Practice of Finite Elements*. Applied Mathematical Sciences. Springer-Verlag, New York, NY, 2004.
- [EH12] K. Eppler and H. Harbrecht. On a Kohn-Vogelius like formulation of free boundary problems. *Comput. Optim. App.*, 52:69–85, 2012.
- [EHLW20] T. Etling, R. Herzog, E. Loayza, and G. Wachsmuth. First and second order shape optimization based on restricted mesh deformations. *SIAM J. Sci. Comput.*, 42(2):A1200–A1225, 2020.
- [ET76] I. Ekeland and R. Temam. *Convex Analysis and Variational Problems*. North-Holland Publishing Co., Amsterdam. Translated from the French, Studies in Mathematics and its Applications, Vol. 1., 1976.
- [Eva10] Lawrence C. Evans. *Partial Differential Equations*. Graduate Series in Mathematics. AMS, 2nd edition, 2010.
- [GCH17] R. Gong, X. Cheng, and W. Han. A coupled complex boundary method for an inverse conductivity problem with one measurement. *Appl. Anal.*, 96(5):869–885, 2017.
- [GK07] C. Gope and N. Kehtarnavaz. Affine invariant comparison of point-sets using convex hulls and hausdorff distances. *Pattern Recognition*, 40:309–320, 2007.
- [GLR24] W. Gong, B. Li, and Q. Rao. Convergent evolving finite element approximations of boundary evolution under shape gradient flow. *IMA J. Numer. Anal.*, 44(5):2667–2697, 2024.
- [GLZ22] W. Gong, J. Li, and S. Zhu. Improved discrete boundary type shape gradients for PDE-constrained shape optimization. *SIAM J. Sci. Comput.*, 44:A2464–A2505, 2022.
- [GZ21] W. Gong and S. Zhu. On discrete shape gradients of boundary type for PDE-constrained shape optimization. *SIAM J. Numer. Anal.*, 59:1510–1541, 2021.
- [HH21] Y. He and W. Huang. Mesh sensitivity analysis for finite element solution of linear elliptic partial differential equations. arXiv:2111.10935, November 2021.
- [HK18] W. Huang and L. Kamenski. On the mesh nonsingularity of the moving mesh pde method. *Math. Comput.*, 87(312):1887–1911, 2018.
- [HM03] J. Haslinger and R. A. E. Mäkinen. *Introduction to Shape Optimization: Theory, Approximation, and Computation*. SIAM, Philadelphia, 2003.
- [HP18] A. Henrot and M. Pierre. *Shape Variation and Optimization: A Geometrical Analysis*, volume 28 of *Tracts in Mathematics*. European Mathematical Society, Zürich, 2018.
- [HPS15] R. Hiptmair, A. Paganini, and S. Sargheini. Comparison of approximate shape gradients. *BIT Numer. Math.*, 55:459–485, 2015.
- [IJT11] K. Ito, B. Jin, and T. Takeuchi. A regularization parameter for nonsmooth Tikhonov regularization. *SIAM J. Sci. Comput.*, 33:1415–1438, 2011.
- [IKP06] K. Ito, K. Kunisch, and G. H. Peichl. Variational approach to shape derivative for a class of Bernoulli problem. *J. Math. Anal. Appl.*, 314(2):126–149, 2006.
- [IKP08] K. Ito, K. Kunisch, and G. H. Peichl. Variational approach to shape derivatives. *ESAIM Control Optim. Calc. Var.*, 14:517–539, 2008.
- [KKBS22] J. P. Knapp, J. E. Kakish, B. W. Bridle, and D. J. Speicher. Tumor temperature: Friend or foe of virus-based cancer immunotherapy. *Biomedicines*, 10(8), 2022.
- [KV87] R. Kohn and M. Vogelius. Relaxation of a variational method for impedance computed tomography. *Commun. Pure Appl. Math.*, 40(6):745–777, 1987.
- [Lau20] A. Laurain. Distributed and boundary expressions of first and second order shape derivatives in nonsmooth domains. *J. Math. Pures Appl.*, 134:328–368, 2020.
- [Law56] R. N. Lawson. Implications of surface temperatures in the diagnosis of breast cancer. *Can. Med. Assoc. J.*, 75:309–310, 1956.
- [LC63] R. N. Lawson and M. S. Chughtai. Breast cancer and body temperatures. *Can. Med. Assoc. J.*, 88:68–70, 1963.
- [LH17] X. Li and W. Huang. A study on nonnegativity preservation in finite element approximation of Nagumo-type nonlinear differential equations. *Appl. Math. Comput.*, 309:49–67, 2017.
- [LS16] A. Laurain and K. Sturm. Distributed shape derivative via averaged adjoint method and applications. *ESAIM Math. Model. Numer. Anal.*, 50:1241–1267, 2016.
- [LZ19] J. Li and S. Zhu. Shape identification in Stokes flow with distributed shape gradients. *Appl. Math. Lett.*, 95:165–171, 2019.
- [LZ22] J. Li and S. Zhu. On distributed  $H^1$  shape gradient flows in optimal shape design of Stokes flows: convergence analysis and numerical applications. *J. Comput. Math.*, 40(2):232–258, 2022.
- [LZ23] J. Li and S. Zhu. Shape optimization of the Stokes eigenvalue problem. *SIAM J. Sci. Comput.*, 45(2):A798–A828, 2023.
- [LZS23] J. Li, S. Zhu, and X. Shen. On mixed finite element approximations of shape gradients in shape optimization with the Navier–Stokes equation. *Numer. Methods Partial Differ. Equ.*, 39(2):1604–1634, 2023.

- [MB95] M. Miyakawa and J. C. Bolomey. *Non-invasive thermometry of the human body*. CRC Press, Boca Raton, FL, 1995.
- [Mef21] H. Meftahi. Uniqueness, Lipschitz stability, and reconstruction for the inverse optical tomography problem. *SIAM J. Math. Anal.*, 53(6):6326–6354, 2021.
- [MP01] B. Mohammadi and O. Pironneau. *Applied Shape Optimization for Fluids*. Clarendon press, Oxford, 2001.
- [MS76] F. Murat and J. Simon. Sur le contrôle par un domaine géométrique. Research report 76015, Univ. Pierre et Marie Curie, Paris, 1976.
- [Neu97] J. W. Neuberger. *Sobolev Gradients and Differential Equations*. Springer-Verlag, Berlin, 1997.
- [OCNN22] H. Ouaiassa, A. Chakib, A. Nachaoui, and M. Nachaoui. On numerical approaches for solving an inverse Cauchy Stokes problem. *Appl. Math. Optim.*, 85(Art. 3):37 pp., 2022.
- [Pag14] A. Paganini. Approximative shape gradients for interface problems. Technical Report 2014-12, Seminar for Applied Mathematics, ETH, Zürich, 2014.
- [Pen48] H. Pennes. Analysis of tissue and arterial blood temperature in the resting human forearm. *J. Appl. Physiol.*, 1(1):93–122, 1948.
- [PH16] A. Paganini and R. Hiptmair. *Approximate Riesz representatives of shape gradients*. System Modeling and Optimization. Springer International Publishing, Cham, 2016.
- [PM07] M. Paruch and E. Majchrzak. Identification of tumor region parameters using evolutionary algorithm and multiple reciprocity boundary element method. *Eng. Appl. Artif. Intell.*, 20:647–655, 2007.
- [RA18] J. F. T. Rabago and H. Azegami. Shape optimization approach to defect-shape identification with convective boundary condition via partial boundary measurement. *Japan J. Indust. Appl. Math.*, 31(1):131–176, 2018.
- [RA20] J. F. T. Rabago and H. Azegami. A second-order shape optimization algorithm for solving the exterior Bernoulli free boundary problem using a new boundary cost functional. *Comput. Optim. Appl.*, 77(1):251–305, 2020.
- [Rab23a] J. F. T. Rabago. Numerical solution to the exterior Bernoulli problem using the Dirichlet-Robin energy gap cost functional approach in two and three dimensions. *Numer. Algorithms*, 94:175–227, February 2023.
- [Rab23b] J. F. T. Rabago. On the new coupled complex boundary method in shape optimization framework for solving stationary free boundary problems. *Math. Control Relat. Fields*, 13(4):1362–1398, 2023.
- [RAN25] J. F. T. Rabago, L. Afraites, and H. Notsu. Detecting immersed obstacle in Stokes fluid flow using the coupled complex boundary method. *SIAM J. Control & Optim.*, page to appear, 2025.
- [RN24] J. F. T. Rabago and H. Notsu. Numerical solution to a free boundary problem for the Stokes equation using the coupled complex boundary method in shape optimization setting. *Appl. Math. Optim.*, 89:Art. 2, 2024.
- [SLR<sup>+</sup>84] C. W. Song, A. Lokshina, J. G. Rhe, M. Patten, and S. H. Levitt. Implication of blood flow in hyperthermic treatment of tumors. *IEEE Trans. Biomed. Eng.*, 31:9–16, 1984.
- [SSW15] V. Schulz, M. Siebenborn, and K. Welker. Structured inverse modeling in parabolic diffusion problems. *SIAM J. Control Optim.*, 53:3319–3338, 2015.
- [Stu16] K. Sturm. *On shape optimization with non-linear partial differential equations*. PhD thesis, Technische Universität Berlin, Berlin, 2016.
- [SZ92] J. Sokolowski and J.-P. Zolésio. *Introduction to Shape Optimization: Shape Sensitivity Analysis*. Springer Series in Computational Mathematics. Springer-Verlag, Berlin, Heidelberg, 1992.
- [ZCG20] X. Zheng, X. Cheng, and R. Gong. A coupled complex boundary method for parameter identification in elliptic problems. *Int. J. Comput. Math.*, 97(5):998–1015, 2020.
- [Zhu18] S. Zhu. Effective shape optimization of Laplace eigenvalue problems using domain expressions of eulerian derivatives. *J. Optim. Theory Appl.*, 176:17–34, 2018.

## APPENDIX A. APPENDICES

**A. Correa-Seeger Theorem.** Let  $\varepsilon > 0$  be a fixed real number and consider a functional

$$F : [0, \varepsilon] \times X \times Y \rightarrow \mathbb{R},$$

for some topological spaces  $X$  and  $Y$ . For each  $t \in [0, \varepsilon]$ , we define

$$M(t) := \min_{x \in X} \sup_{y \in Y} F(t, x, y) \quad \text{and} \quad m(t) := \sup_{y \in Y} \min_{x \in X} F(t, x, y),$$

and the associated sets

$$X(t) := \left\{ \hat{x} \in X \mid \sup_{y \in Y} F(t, \hat{x}, y) = M(t) \right\}$$

$$Y(t) := \left\{ \hat{y} \in Y \mid \min_{x \in X} F(t, x, \hat{y}) = m(t) \right\}.$$

We introduce the *set of saddle points*

$$S(t) = \{(\hat{x}, \hat{y}) \in X \times Y : M(t) = F(t, \hat{x}, \hat{y}) = m(t)\},$$

which may be empty. In general, we always have the inequality  $m(t) \leq M(t)$ , and when  $m(t) = M(t)$ , the set  $S(t)$  is exactly  $X(t) \times Y(t)$ .

We quote below an improved version of Correa-Seeger theorem stated in [DZ11, Thm. 5.1, pp. 556–559].

**Theorem A.1** (Correa and Seeger, [CS85]). *Let the sets  $X$  and  $Y$ , the real number  $\varepsilon > 0$ , and the functional  $F : [0, \varepsilon] \times X \times Y \rightarrow \mathbb{R}$  be given. Assume that the following assumptions hold:*

- (H1): *for  $0 \leq t \leq \varepsilon$ , the set  $S(t)$  is non-empty;*
- (H2): *the partial derivative  $\partial_t F(t, x, y)$  exists everywhere in  $[0, \varepsilon]$ , for all  $(x, y) \in \left[ \bigcup_{t \in [0, \varepsilon]} X(t) \times Y(0) \right] \cup \left[ X(0) \times \bigcup_{t \in [0, \varepsilon]} Y(t) \right]$ ;*
- (H3): *there exists a topology  $\mathcal{T}_X$  on  $X$  such that for any sequence  $\{t_n : 0 < t_n \leq \varepsilon\}$ ,  $t_n \rightarrow t_0 = 0$ , there exist an  $x^0 \in X(0)$  and a subsequence  $\{t_{n_k}\}$  of  $\{t_n\}$ , and for each  $k \geq 1$ , there exists  $x_{n_k} \in X(t_{n_k})$  such that (i)  $x_{n_k} \rightarrow x^0$  in the  $\mathcal{T}_X$ -topology, and (ii) for all  $y$  in  $Y(0)$ ,  $\liminf_{t \searrow 0, k \rightarrow \infty} \partial_t F(t, x_{n_k}, y) \geq \partial_t F(0, x^0, y)$ ;*
- (H4): *there exists a topology  $\mathcal{T}_Y$  on  $Y$  such that for any sequence  $\{t_n : 0 < t_n \leq \varepsilon\}$ ,  $t_n \rightarrow t_0 = 0$ , there exist  $y^0 \in Y(0)$  and a subsequence  $\{t_{n_k}\}$  of  $\{t_n\}$ , and for each  $k \geq 1$ , there exists  $y_{n_k} \in Y(t_{n_k})$  such that (i)  $y_{n_k} \rightarrow y^0$  in the  $\mathcal{T}_Y$ -topology, and (ii) for all  $x$  in  $X(0)$ ,  $\limsup_{t \searrow 0, k \rightarrow \infty} \partial_t F(t, x, y_{n_k}) \leq \partial_t F(0, x, y^0)$ ;*

Then, there exists  $(x^0, y^0) \in X(0) \times Y(0)$  such that

$$dM(0) = \min_{x \in X(0)} \sup_{y \in Y(0)} \partial_t F(0, x, y) = \partial_t F(0, x^0, y^0) = \sup_{y \in Y(0)} \min_{x \in X(0)} \partial_t F(0, x, y).$$

Thus,  $(x^0, y^0)$  is a saddle point of  $\partial_t F(0, x, y)$  on  $X(0) \times Y(0)$ .

**B. Material derivative of the state.** This appendix describes the structure of the *material derivative of the state*, defined as follows (see, e.g., [SZ92, Eq. (3.38), p. 111]):

$$\dot{u} = \dot{u}(\Omega)[\theta] = \lim_{t \searrow 0} \frac{u(\Omega_t) \circ T_t - u(\Omega)}{t} \quad (\text{B.73})$$

provided that the limit  $\dot{u}$  exists in  $H^1(\Omega)$ , where  $(u(\Omega_t) \circ T_t)(x) = u(\Omega_t)(T_t(x))$ ,  $x \in \Omega$ .

To simplify the computation, we assume  $C^{1,1}$  bounded domains and sufficiently regular coefficients in (2). By a classical elliptic regularity result (see, e.g., [Eva10]), the state is also  $H^2(\Omega)$ -regular. If  $\Omega$  is a Lipschitz domain, then  $u$  belongs globally to  $H^1(\Omega)$ . However, locally,  $u$  has improved regularity:  $u_1 \in H^2(\Omega_\circ \setminus \overline{\Omega}_0)$  and  $u_0 \in H^2(\Omega_0)$ .

We assume the following strong assumptions:

**Assumption A.2.** *We assume that*

- $\Omega \subset \mathbb{R}^d$ ,  $d \in \{2, 3\}$ , is admissible;
- $\sigma_0, \sigma_1 \in C^1(\overline{\Omega})$  and  $\sigma_0, \sigma_1 > 0$ ;
- $k_0, k_1 \in C^1(\overline{\Omega})$  and  $k_0, k_1 > 0$ ;
- $Q_0, Q_1 \in C^1(\overline{\Omega})$ .

In this section, we will assume  $T_a \in \mathbb{R}_+$  and  $T_b \equiv 0$  to simplify the computations and arguments. Note that for the general case where  $T_b > 0$ , the linear form  $a(u_b, v)$ ,  $u_b \in H^1(\Omega)$ ,  $v \in V(\Omega)$  must be included in the calculations.

**Theorem A.3.** *Let  $\Omega \in \Upsilon^1$ ,  $\theta \in \Theta^1$  and assume that Assumption A.2 holds. Then, the state  $u = u(\Omega) \in V(\Omega)$ , has the material derivative  $\dot{u} \in V(\Omega)$  satisfying the following variational*

equation

$$\begin{aligned} a(\dot{u}, v) &= - \sum_{j=0}^1 \int_{\Omega_j} [\nabla \sigma_j \cdot \theta(\nabla u \cdot \nabla v) + \nabla k_j \cdot \theta uv - \nabla Q_j \cdot \theta v] dx \\ &\quad - \sum_{j=0}^1 \int_{\Omega_j} [\sigma_j A \nabla u \cdot \nabla v + \operatorname{div} \theta k_j uv + \operatorname{div} \theta Q_j v] dx, \quad \forall v \in V(\Omega), \end{aligned} \quad (\text{B.74})$$

where the sesquilinear form  $a(\cdot, \cdot)$  is given by (10) and  $A = (\operatorname{div} \theta)I - D\theta - (D\theta)^\top$ .

*Proof.* In the proof, we do not split the integrals over the sub-domains  $\Omega_1$  and  $\Omega_0$  for notational convenience.

Let the assumptions of the assertion be satisfied. Let us consider  $u_t \in V(\Omega_t) := H^1(\Omega_t)$ , the solution of the perturbed problem for a given variation  $\theta \in \Theta^1$  is given by the solution of

$$a_t(u_t, v_t) = l_t(v_t), \quad \forall v_t \in V(\Omega_t). \quad (\text{B.75})$$

where

$$\begin{aligned} a_t(u_t, v) &:= \int_{\Omega_t} (\sigma_t \nabla u_t \cdot \nabla \bar{v} k_t u_t \bar{v}) dx_t + \int_{\Gamma_u} (\alpha + i) u_t \bar{v} ds, \\ l_t(v) &:= \int_{\Omega_t} Q_t \bar{v} dx_t + \int_{\Gamma_{u,t}} (\alpha T_a + ih) \bar{v} ds. \end{aligned}$$

Here,  $\sigma_t = \sigma_{1,t} \chi_{\Omega \setminus \bar{\Omega}_{0,t}} + \sigma_{0,t} \chi_{\Omega_{0,t}}$ ,  $\kappa_t = \kappa_{1,t} \chi_{\Omega \setminus \bar{\Omega}_{0,t}} + \kappa_{0,t} \chi_{\Omega_{0,t}}$ , and  $Q = Q_{1,t} \chi_{\Omega \setminus \bar{\Omega}_{0,t}} + Q_{0,t} \chi_{\Omega_{0,t}}$ , where  $\chi_{(\cdot)}$  denotes the characteristic function. The change of variables (cf. [DZ11, subsec. 9.4.2–9.4.3, pp. 482–484]) allows us to rewrite (B.75) as follows:

$$a^t(u^t, v) = l^t(v), \quad \forall v \in V(\Omega),$$

where

$$\begin{cases} a^t(u^t, v) = \int_{\Omega} (\sigma_t A_t \nabla u^t \cdot \nabla v + I_t k^t u^t v) dx + \int_{\Gamma_u} b_t (\alpha + i) u^t v ds, & \text{for } u^t, v \in V(\Omega), \\ l^t(v) = \int_{\Omega} I_t Q^t v dx + \int_{\Gamma_u} b_t (\alpha T_a + ih) v ds, & \text{for } v \in V, \quad (\varphi^t = \varphi_t \circ T_t : \Omega \rightarrow \mathbb{R}). \end{cases}$$

We underline here that on  $\partial\Omega = \Gamma_u \cup \Gamma_w \cup \Gamma_b$ ,  $b_t = I_t |(DT_t)^{-\top} n| = 1$  because  $\theta|_{\partial\Omega} = 0$ .

Using the properties of  $T_t$  from (16) and the bounds from (18), it can be shown that  $w^t = u^t - u \in V(\Omega)$  is the unique solution to the variational equation  $a^\top(u^t, v) - a(u, v) = l^\top(v) - l(v)$  for all  $v \in V(\Omega)$ . This equation can also be written as:

$$\tilde{a}(w^t, v) = \tilde{l}(v), \quad \forall v \in V(\Omega), \quad (\text{B.76})$$

where

$$\begin{cases} \tilde{a}(w^t, v) = \int_{\Omega} (\sigma_t \nabla w^t \cdot \nabla v + k^t w^t v) dx + \int_{\Gamma_u} (\alpha + i) w^t v ds, & w^t, v \in V(\Omega), \\ \tilde{l}(v) = - \int_{\Omega} (\sigma_t - \sigma) A_t \nabla u^t \cdot \nabla v dx - \int_{\Omega} \sigma (A_t - I) \nabla u^t \cdot \nabla v dx \\ \quad - \int_{\Omega} I_t (k^t - k) u^t v dx - \int_{\Omega} (I_t - 1) k u^t v dx \\ \quad + \int_{\Omega} I_t (Q^t - Q) v dx + \int_{\Omega} (I_t - 1) Q v dx, & u^t, v \in V(\Omega). \end{cases} \quad (\text{B.77})$$

For all  $t \in \mathbb{I}$ , the well-posedness of (B.76) follows from the complex version of the Lax-Milgram theorem [DL98, p. 376], using standard arguments along with the uniform boundedness of  $\{A_t\}$  and  $\{I_t\}$  on  $\Omega$ , as well as the regularity of the coefficients and data given in Assumption A.2. As a result, we obtain  $\|w^t\|_V \lesssim \|u\|_V$ , for  $t \in \mathbb{I}$ . Thus, the set  $\{w^t \mid t \in \mathbb{I}\}$  is bounded in  $V$ .



Let us define  $z^t = \frac{1}{t}w^t$  for  $t \in (0, t_0)$  which also belongs to  $V$ . Then, we have

$$\begin{aligned} \tilde{a}(z^t, v) &= - \int_{\Omega} \left( \frac{\sigma_t - \sigma}{t} \right) A_t \nabla u^t \cdot \nabla v \, dx - \int_{\Omega} \sigma \left( \frac{A_t - I}{t} \right) \nabla u^t \cdot \nabla v \, dx \\ &\quad - \int_{\Omega} I_t \left( \frac{k^t - k}{t} \right) u^t v \, dx - \int_{\Omega} \left( \frac{I_t - 1}{t} \right) k u^t v \, dx \\ &\quad + \int_{\Omega} I_t \left( \frac{Q^t - Q}{t} \right) v \, dx + \int_{\Omega} \left( \frac{I_t - 1}{t} \right) Q v \, dx = \frac{1}{t} \tilde{l}(v) =: l_t(v), \quad (v \in V(\Omega)). \end{aligned}$$

By choosing  $v = z^t$  above, we deduce that  $z^t$  is bounded in  $V$ . Thus, there exists a sequence  $\{t_n\}$  (taking a subsequence if necessary) that converges to zero and an element  $z \in V(\Omega)$  such that  $z^{t_n} \rightharpoonup z$  weakly in  $V$ . Since  $\nabla u^{t_n} \rightarrow \nabla u$  in  $L^2(\Omega)^d$  and  $I_{t_n} \rightarrow 1$  and  $A_{t_n} \rightarrow I$  uniformly on  $\Omega$  as  $n \rightarrow \infty$ , we conclude, by (17) and [IKP06, Cor. 3.1], that

$$\begin{aligned} a_0(z, v) &:= \int_{\Omega} (\sigma \nabla z \cdot \nabla v + k z v) \, dx + \int_{\Gamma_u} (\alpha + i) z v \, ds \\ &= - \int_{\Omega} (\nabla \sigma \cdot \theta(\nabla u \cdot \nabla v) + \sigma A \nabla u \cdot \nabla v) \, dx - \int_{\Omega} (\nabla k \cdot \theta u v + \operatorname{div} \theta k u v) \, dx \\ &\quad + \int_{\Omega} (\nabla Q \cdot \theta v + \operatorname{div} \theta Q v) \, dx =: l_1(v) + l_2(v) + l_3(v) =: l_0(v), \quad (\forall v \in V(\Omega)). \end{aligned}$$

Since this equation has a unique solution, we conclude that the sequence  $\{z^{t_n}\}$  weakly converges to  $z$  in  $V$  for any sequence  $\{t_n\}$  converging to zero. Moreover, the strong convergence follows from  $a_0(z, z) = \lim_{t_n \searrow 0} \tilde{a}(z^{t_n}, z^{t_n}) = \lim_{t_n \searrow 0} l_{t_n}(z^{t_n}) = l_0(z)$ , together with the previously established weak convergence. This confirms that the unique material derivative  $z = \dot{u} \in V(\Omega)$  of  $u \in V(\Omega)$  is characterized as in (B.74).  $\square$

### C. Proof of Lemma 6.1.

*Proof of Lemma 6.1.* Evidently, from (33),  $\nabla \lambda_i$  is a (non-zero) constant vector. Let us define  $\mathbf{a}_i$  as the  $i$ th height of  $K$ , measured from the  $i$ th vertex  $x_i$  to the opposite facet or edge  $F_i$ , and  $\mathbf{a}_K$  be the smallest among these heights. So,  $F_i$  is essentially the base of the triangle  $K$  with respect to the  $x_i$ . Let us define  $x_i^\perp$  as the foot of the altitude of  $x_i$  and  $n_i^\perp$  as the unit vector perpendicular to the base and pointing from the base toward the vertex  $x_i$ . Accordingly, we may write  $\mathbf{a}_i = \overrightarrow{|(x_i x_i^\perp)|} = |x_i - x_i^\perp|$ . Recall that  $\lambda_i$  is affine. So, we may write  $\lambda_i(x) = \lambda_i(x_i^\perp) + \nabla \lambda_i \cdot \overrightarrow{(x x_i^\perp)}$ , for any point  $x$ . In particular, we have

$$\nabla \lambda_i \cdot \overrightarrow{(x_i x_i^\perp)} = \lambda_i(x_i) - \lambda_i(x_i^\perp).$$

Let us recall that  $\lambda_i$  vanishes at any point on  $F_i$ , and obviously,  $x_i^\perp \in F_i$ . So,  $\lambda_i(x_i^\perp) = 0$ . In addition, we have  $\lambda_i(x_i) = 1$  by definition. Note also that, by definition,  $n_i^\perp = \frac{x_i - x_i^\perp}{|x_i - x_i^\perp|}$ . Therefore, we see that

$$\nabla \lambda_i = \frac{\lambda_i(x_i) - \lambda_i(x_i^\perp)}{|x_i - x_i^\perp|} = \frac{1}{\overrightarrow{|(x_i x_i^\perp)|}} = r n_i^\perp,$$

for some scalar  $r$ , and  $\nabla \lambda_i \parallel n_i^\perp$ . Thus, we obtain

$$|\nabla \lambda_i| \overrightarrow{|(x x_i^\perp)|} \cos(0) = \nabla \lambda_i \cdot \overrightarrow{(x x_i^\perp)} = \lambda_i(x) = 1, \quad \text{or equivalently,} \quad a_i = \frac{1}{|\nabla \lambda_i|},$$

for  $i = 1, 2, 3$ , proving the lemma.  $\square$